Precision Deuteron Charge Radius Measurement with Elastic Electron-Deuteron Scattering

A. Gasparian (spokesperson and contact person), M. Levillain, R. Pedroni
North Carolina A&T State University, Greensboro, NC 27411

I. Akushevich, H. Gao (co-spokesperson), C. Gu, X. Li, T. Liu, C. Peng, W. Xiong, X. Yan, Y. Zhang, Z. Zhao
Duke University, Durham, NC 27708

K. Adhikari, K. Assumin-Gyimah, H. Bhatt, D. Bhetuwal, J. Dunne, D. Dutta (co-spokesperson), L. El-Fassi, L. Kabir, A. Karki, M. Shabestari, L. Ye
Mississippi State University, Miss State, MS 39762

X. Bai, D. Di, S. Jian, N. Liyanage (co-spokesperson), K. Gnanvo, J. Matter, V. Nelyubin, H. Nguyen
University of Virginia, Charlottesville, VA 22904

J. Brock, C. Carlin, D. Gaskell, Y. Gotra, D. Higinbotham, C. Keith, J. Maxwell, D. Meekins, E. Pasyuk (co-spokesperson), S. Stepanyan, B. Wojtsekhowski
Thomas Jefferson National Accelerator Facility, Newport News, VA 23606

M. Khandaker
Idaho State University, Pocatello, ID 83209

L. Gan
University of North Carolina Wilmington, NC 28403

A. V. Gramolin
Budker Institute of Nuclear Physics, Novosibirsk, Russia

I. Larin, R. Miskimen
University of Massachusetts, Amherst, MA 01003

A. Dolgolenko, V. Goryachev, V. Matveev, V. Tarasov
ITEP, Moscow, Russia

And
The PRad Collaboration

Abstract

Recent high precision deuteron rms charge radius measurements performed by the CREMA collaboration at PSI using spectroscopy of muonic deuterium atom demonstrated a $\sim 7\sigma$ discrepancy with the long-established CODATA world-average value, creating a new *"deuteron charge radius puzzle"* in hadronic physics. We propose to perform a new high precision elastic ed scattering cross section measurement at very low scattering angles, $\theta_e = 0.7^\circ - 6.0^\circ$ (Q^2= 2×10^{-4} to 5×10^{-2} $(\mathrm{GeV/c})^2$) at $E_0 = 1.1$ and 2.2 GeV, using the PRad experimental setup with two major modifications. To ensure the elasticity of the ed scattering process we will add a low energy Si-based cylindrical recoil detector within the windowless gas flow target cell. We also propose to add a second pair of GEM chambers in front of the HyCal calorimeter to significantly improve the tracking capability enabling vertex reconstruction for better control of the beam-line background. As in the PRad experiment, to control the systematic uncertainties associated with measuring the absolute ed cross section, a well known QED process, the ee Møller scattering will be simultaneously measured in this experiment. The proposed experiment will allow a sub-percent (0.5%) and essentially model independent extraction of the deuteron charge radius to address the newly developed *"deuteron charge radius puzzle"*.

Contents

1 Introduction

Elastic electron scattering has been a well established tool to determine the radii of nuclear charge distributions. The unique advantage of electron scattering is that, the well understood electromagnetic interaction being weak enables the separation of the scattering process from the effects of the strong nuclear force and other nuclear properties. The availability of intense and precisely controlled electron beams, such as the CW electron beam at Jefferson Lab, allows for very accurate measurements of the nuclear charge distributions. The charge radii of the lightest nuclei can also be extracted from laser spectroscopy of atomic hydrogen (H) and deuterium (D). The radii extracted from electron scattering and atomic spectroscopy were typically found to be consistent within experimental uncertainties. This allowed them to be combined together to obtain a "world average" value of the proton (r_p) and deuteron (r_d) root mean square (rms) charge radius, by a self-consistent least-squares adjustment of the fundamental physical constants, published in the most recent CODATA compilation [1]. However, recently the most precise radii have been obtained from the spectroscopy of muonic atoms [2, 3, 4]. The radii obtained from these ultra-precise muonic atom measurements were found to be inconsistent with the CODATA values, as shown in Fig 1. For example, the $\sim 7\ \sigma$ discrepancy between the CODATA and the muonic spectroscopy values for the proton charge radius gave rise to the "*Proton Radius Puzzle*" [5, 6]. A similar, more than $\sim 7\ \sigma$, discrepancy between the deuteron charge radius from spectroscopy of muonic deuterium and the CODATA value was reported recently [4]. It is tempting to dismiss such comparisons between r_p and r_d as redundant because the CODATA values of the two are highly correlated [1]. The large correlation is the result of the very precisely measured isotope shift of the $1S \rightarrow 2S$ transition in H and D obtained from cyclotron frequency measurements in a Penning trap [7, 8]. The accurately known isotope shift then yields a very accurate value for the difference of the (squared) deuteron and proton charge radii: $r_d^2 - r_p^2 = 3.82007(65)$ [9], which along with the elastic electron scattering on protons and deuterons determine the CODATA values of r_p and r_d respectively. Thus, it can be argued that the CODATA deuteron charge radius is larger than the muonic deuterium value only because the highly correlated and accurately determined proton charge radius is larger than the muonic hydrogen value. But, a recent re-analysis of the existing data from atomic deuterium spectroscopy was used to deduce a deuteron charge radius without relying on the value of the proton charge radius [10]. The newly deduced value is in excellent agreement with the CODATA value but still $\sim 3.5\ \sigma$ larger than the value obtained from muonic deuterium. This indicates that in addition to the "*Proton Radius Puzzle*" there also exists a "*Deuteron Radius Puzzle*".

In order to address the "*Proton Radius Puzzle*", PRad, a new high precision electron scattering experiment, was recently completed at JLab. This experiment included several unique features such as a new windowless cryo-cooled hydrogen gas flow target, a magnetic spectrometer free design using a high resolution electromagnetic calorimeter (HyCal) which allowed the experiment to reach the lowest four momentum transfer squared (Q^2) amongst electron scattering experiments. Two large area gas electron multiplier (GEM) chambers were also used to help improve the angular resolution. Finally, the simultaneous detection of Møller and elastic electron-proton (e-p) scattering events within the same experimental acceptance helped reduce many systematic uncertainties. The PRad experiment successfully completed data collection in June 2016 and currently data analysis is underway. The success of all of the unique features of the PRad experiment demonstrated the superiority of this technique. Based on the experience gained during the PRad experiment we are proposing a new set of measurements on deuterium using the same technique, but with an upgraded setup. The proposed experiment will enable the most precise measurement of the deuteron charge radius using electron scattering, with the ultimate goal of resolving the "*Deuteron Radius Puzzles*".

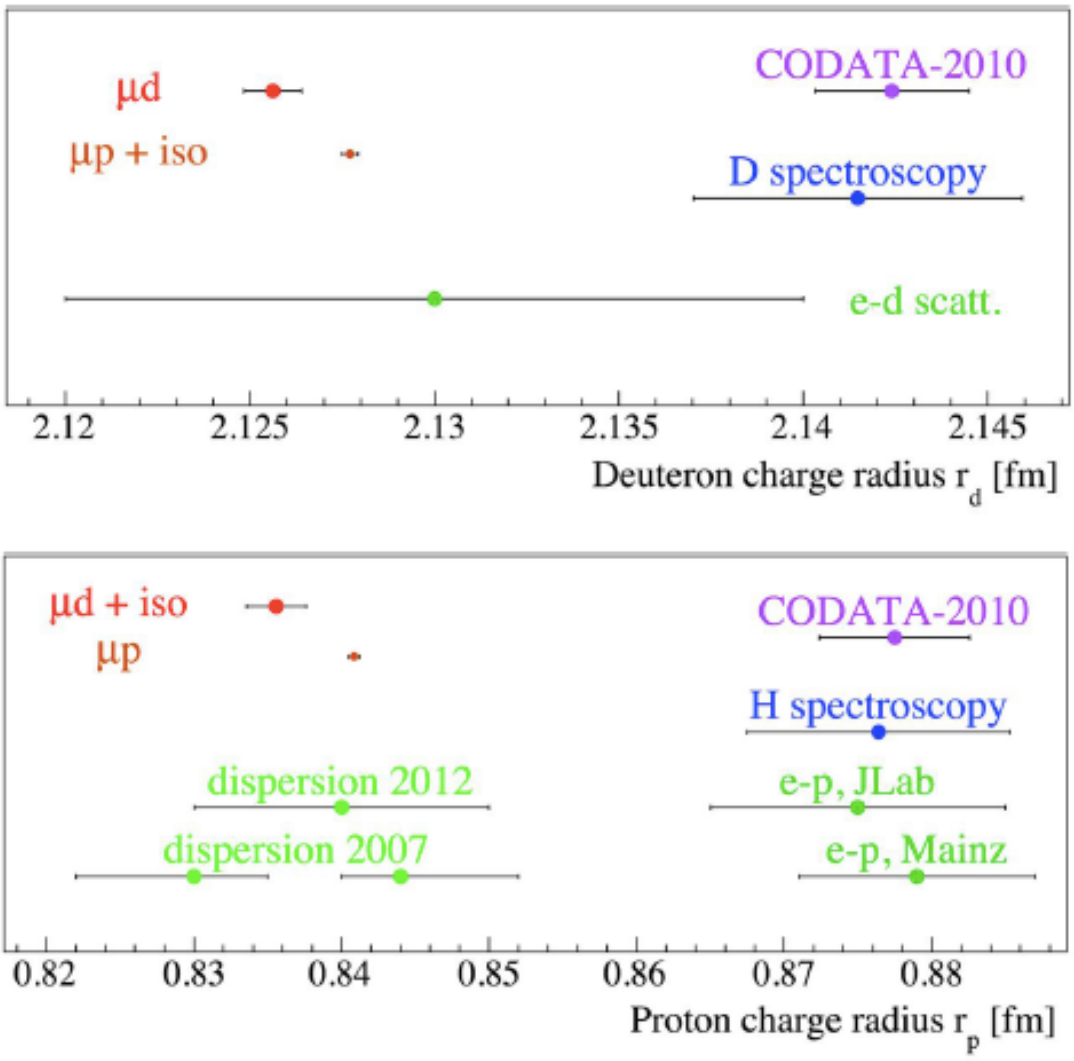

Figure 1: The CODATA values for the deuteron charge radius (top) and proton charge radius (bottom), along with measurements using spectroscopy of muonic atoms, electron scattering and atomic spectroscopy, reproduced from Ref. [4]. The point labeled as D-spectroscopy (top) is the deuteron charge radius from just deuteron spectroscopy without using the proton charge radius as described in Ref. [10].

2 Physics Motivation

As the only bound two-nucleon system, the deuteron is of fundamental importance to nuclear physics and has been studied extensively both experimentally and theoretically. The wave function of the deuteron can be calculated accurately for a variety of nucleon-nucleon (NN) potentials. It is expected that at very low momentum transfer Q, where the non-nucleonic degrees of freedom and relativistic corrections are negligible, the electromagnetic properties of the deuteron, can be accurately predicted. The deuteron form factors at low Q are dominated by the parts of the deuteron wave function for which the two nucleons are far apart, and hence the deuteron's electromagnetic properties such as its rms charge radius should be determined just by the nucleon-nucleon (NN) interaction and the nucleon form factors, both of which are

well known. The theoretical calculations of the rms radius of the deuteron are considered reliable as they are independent of the NN potential for a broad class of potentials and depends mostly on its well known binding energy and n-p scattering length [11]. This is why the deuteron rms radius is an ideal observable to compare experiments with theory.

2.1 Radius from Electron Scattering

The earliest experimental knowledge on the deuteron rms charge radius came from elastic electron-deuteron (e-d) scattering [12]. Although, e-d elastic scattering was first studied to learn about the neutron form factors, they were also used to extract the deuteron rms charge radius. In the Born approximation the cross section for elastic scattering from a nuclear target is given by [13];

$$\frac{d\sigma}{d\Omega} = \frac{d\sigma}{d\Omega}|_{NS}[A(Q^2) + B(Q^2)\tan^2\theta/2], \tag{1}$$

where $\frac{d\sigma}{d\Omega}|_{NS}$ is the cross section for the elastic scattering from a point-like and spinless particle with the mass of the nucleus, at electron incident energy of E_0, and, scattering angle θ. The structure functions $A(Q^2)$ and $B(Q^2)$ are related to the deuteron charge, electric quadrupole and magnetic dipole form factors G_{Cd}, G_{Qd} and G_{Md} respectively, as [14, 15];

$$\begin{aligned} A(Q^2) &= G_{Cd}^2(Q^2) + \frac{2}{3}\eta G_{Md}^2(Q^2) + \frac{8}{9}\eta^2 G_{Qd}^2(Q^2) \\ B(Q^2) &= \frac{4}{3}\eta(1+\eta)G_{Md}^2(Q^2), \end{aligned} \tag{2}$$

where $\eta = Q^2/4m_d^2$, the deuteron mass is given by m_d, $G_{Cd}(0) = 1, G_{Md}(0)/\mu_{Md} = 1$ and $G_{Qd}(0)/\mu_{Qd} = 1$, with μ_{Md} and μ_{Qd} being the deuteron magnetic moment and quadrupole moment respectively. The two structure functions are separated using the standard Rosenbluth separation method. At low Q^2 the contributions from the magnetic and quadrupole form factors are small and the rms charge radius can be obtained from the slope of the elastic e-d electric structure function $A(Q^2)$ as,

$$r_d^2 = -6[\frac{dA(Q^2)}{dQ^2}]_{Q^2=0}. \tag{3}$$

Information from elastic e-d scattering has been available since 1957 [16], but the overall normalization uncertainty in most measurements up to the mid-seventies was $\sim 5\%$ [17]. Later measurements at Mainz were able to achieve uncertainties below 1% [18]. However the ratio of e-d to e-p scattering can be determined much more precisely, for example an uncertainty of 0.13% on the ratio was reported in Ref. [18]. These ratios of cross sections are used to determine the deuteron rms matter (structure) radius, r_{md} instead of the rms charge radius. This is because the ratio of e-d to e-p scattering cross sections at low Q^2 provide the ratio of the experimental charge form factors, $R(Q^2) = \frac{G_{Cd}(Q^2)}{G_{Ep}(Q^2)}$, where G_{Ep} is the proton electric form factor, and the ratio of charge form factors can also be written as;

$$\frac{G_{Cd}(Q^2)}{G_{Ep}(Q^2)} = \left(1 + \frac{G_{En}}{G_{Ep}}\right)\frac{C_E(Q^2)}{\sqrt{1+\tau}}\frac{1}{1+cQ^2}, \tag{4}$$

where $C_E(Q^2)$ is called the deuteron structure factor and given by $C_E(Q^2) = 1 - \frac{1}{6}r_d^2Q^2 + ...$, $G_{En} = -\frac{dG_{En}}{dQ^2}|_{Q^2=0}Q^2 + ...$, $G_{Ep}(Q^2) = 1 - \frac{1}{6}r_p^2Q^2 + ...$, $\tau = Q^2/4m_p^2$, the factor $1/\sqrt{1+\tau}$ is the relativistic correction and the factor $\frac{1}{1+cQ^2}$ is the correction for non-nucleonic degrees of freedom. Neglecting terms of order Q^4 and higher we get;

$$R(Q^2) = \frac{G_{Cd}(Q^2)}{G_{Ep}(Q^2)} = 1 - \frac{Q^2}{6}r_x^2|_{Q^2=0}, \tag{5}$$

where $r_x^2 = r_{md}^2 + r_n^2 + \frac{3}{4}(\frac{\hbar}{m_p c})^2$, and $r_n^2 = -6\frac{dG_{En}}{dQ^2}|_{Q^2=0}$ is the neutron radius square which is known with high precision from the scattering of thermal neutrons on atomic electrons [19], and the term $\frac{3}{4}(\frac{\hbar}{m_p c})$ represents the relativistic Zitterbewegung corrections. In most analyses the measured ratio of cross sections $R(Q^2)$ is fitted to a polynomial;

$$R(Q^2) = \sum_{n=0}^{N} (-)^n a_n Q^{2n}, \tag{6}$$

and the mean square (ms) radius is deduced from $r_x^2 = 6a_1/a_0$. Finally, one can obtain the ms charge radius as $r_d^2 = r_{md}^2 + r_p^2$, where r_p^2 is the proton charge radius square. Thus, even though the ratio of e-d to e-p cross section is much more precise compared to the absolute e-d scattering cross section, one must use the proton charge radius in order to get the deuteron charge radius.

To date, elastic e-d scattering has been investigated in many experiments which cover a large range of Q (0.2 - 4.0 fm^{-1}), for a brief review see Ref. [20]. The most relevant among these, for rms radius extraction, are three measurements at low Q that have reached the highest accuracy [21, 18, 22]. Berard *et al.* [21] used cooled H_2 and D_2 gas targets to measure the ratio of cross sections relative to hydrogen over a Q range of 0.2-0.7 fm^{-1}. The deuterium cross sections were obtained by normalizing to the absolute cross section data on hydrogen. Simon *et al.* [18] used both gas and liquid targets to cover different ranges in Q, with a net coverage of 0.2-2.0 fm^{-1}. The hydrogen data collected on a gas target using a special small angle spectrometer served as the absolute cross section standard. Finally, Platchkov *et al.* [22] used a liquid deuterium target to cover a range of Q = 0.7 - 4.5 fm^{-1} with data collected on a liquid hydrogen target for absolute cross sections. As noted in Ref. [20] these publications did not adequately discuss all the systematic uncertainties, and sometimes important sources of uncertainty such as electron beam energy, beam halos e.t.c. are not mentioned.

Nonetheless, the extracted deuteron rms radius tended to be consistent with the calculated radius until about 1980 [11]. The situation changed in 1980 when the value of the proton charge radius was revised from the long accepted value of 0.805(11) fm to the new much larger value of 0.862(12) fm as a result of a measurement at Mainz [23]. Using the revised proton radius, the new value of the deuteron rms radius was in serious disagreement with the theoretical values given by the best models of the nuclear forces. This discrepancy between electron scattering results and theoretical calculations led several authors to explore potential corrections such as meson exchange currents [24], dispersive corrections [25], and energy dependence of the NN interaction [26], however the effect on the rms radius from these corrections were found to be very small. In 1996, Sick and Trautmann [27], re-analyzed the world data on e-d scattering and showed that much of the discrepancy originates from the fact that the Coulomb distortions were neglected in the Plane-Wave Born Approximation (PWBA) commonly used to analyze e-d scattering data. Although Coulomb distortions are small ($\sim 1\%$), the distortion effects are significant at the level of precision reported in the extraction of the rms radius. Once the Coulomb distortions were accounted for, the rms deuteron radius determined from electron scattering [20] ($r_d(e,e) = 2.13 \pm 0.01$ fm) was found to be consistent with theoretical calculations, radius determined from NN scattering [28]($r_d(NN) = 2.13 \pm 0.002$), and optical isotope shifts [29]($r_d(iso) = 2.1316 \pm 0.001$), as shown in Fig. 1.

It must be stressed that, all previous extractions of the deuteron charge radius have relied on deuteron cross sections measurements which were normalized to absolute cross section measurements on hydrogen. The 2010 measurement of the proton charge radius using muonic atoms which gave rise to the so called "*Proton Radius Puzzle*", forces us to consider alternative techniques that do not rely on the absolute hydrogen cross section. The normalization uncertainty can be better controlled if the measured cross section and cross section ratios are normalized to a well understood, pure QED cross section such as the Møller scattering cross section, instead of the $e-p$ cross section. The systematic uncertainties of the deuteron rms radius extracted from electron scattering can be further reduced by using an identical target and detector system

to measure both $e-d$ and $e-p$ scattering in a single experiment that can reach lower values of Q^2 than previously achieved but simultaneously cover a wide enough range in Q^2. The measurement proposed here incorporates all of these improvements and allows for a high precision extraction of the deuteron charge radius using two complementary techniques that have completely different, and in our opinion, better, control over systematic uncertainties compared to all previous measurements.

2.2 Radius from Atomic Deuteron Spectroscopy

The deuteron charge radius can also be obtained from the Lamb shift of the energy levels of atomic deuterium. The Lamb shift describes self-energy and other effects not included in the energies calculated from Dirac equation. One of its smaller contributions is the leading order nuclear structure (NS) contribution coming from the nuclear charge distribution acting only on the atomic nS state [30]:

$$L_{NS}(nS) = (Z\alpha)^4 m \frac{2}{3n^3}(mR_N)^2 = 1.566(Z^4/n^3)R_n^2 MHz \tag{7}$$

Here, Z is the nuclear charge, α is the fine structure constant, m is the electron mass, n is the principal quantum number, and R_N is the nuclear rms charge radius. It contributes about 0.888 MHz in the 2S state of deuterium if its charge radius is 2.13 fm. The experimental precision in measuring the Lamb shift in deuterium is currently 1.5 kHz [31], while an ultimate precision that could be orders of magnitude smaller [32]. This indicates that, assuming the accuracy of QED, Lamb-shift measurements can provide very precise information on the deuterium charge radius.

Another commonly used technique involves using the very precisely measured isotope shift of the $1S \rightarrow 2S$ transition in atomic hydrogen and deuterium [33, 34] to obtain a very accurate value of the difference of the squared deuteron and proton charge radii ($r_d^2 - r_p^2 = 3.82007(65)$ fm^2) [35]. This difference along with the proton charge radius extracted from Lamb shift measurements on atomic hydrogen is used to extract the deuteron charge radius. In fact the CODATA-2010 compilation uses only the radii from isotope shifts and from electron scattering in their evaluation of the current best value of the deuteron charge radius, $r_d =$ 2.1424 (21) fm [1].

Recently, Pohl *et al.* [10] have argued that the $1S \rightarrow 2S$ transitions in atomic deuterium have been previously measured [31, 34] with sufficient accuracy to extract the deuteron charge radius directly from these measurements rather than from the isotope shifts. Using these $1S \rightarrow 2S$ transitions they are able to deduce a deuteron charge radius of $r_d = 2.1415(45)$ fm. This value is independent of the proton charge radius and is consistent with the CODATA-2010 value but less accurate by a factor of 2. This is shown as the deuteron spectroscopy only value in Fig. 1.

2.3 Radius from Muonic Atom Spectroscopy

Muonic atoms are a special class of "exotic" atoms that provide access to the charge radius with much higher precision compared to other methods. In a muonic atom, the nucleus is orbited by one negative muon μ^-, instead of the usual electron. The muon's larger mass $m_\mu = 207m_e$ results in a muonic Bohr radius that is smaller than the corresponding electronic Bohr radius by the ratio of the reduced masses, m_{red}. For μd, the $m_{red} = 196m_e$, and as the Bohr radius reduces proportional to $1/m_{red}$, the overlap of the muon's wave function with the nuclear charge distribution increases as m_{red}^3. Hence, the wave function overlap is $\sim 10^7$ larger in μd compared to D. A measurement of the Lamb shift ($2P \rightarrow 2S$ energy difference) in μd is therefore extremely sensitive to the deuteron charge radius.

The CREMA collaboration has recently reported a deuteron charge radius $r_d = 2.12562(78)$ fm, extracted from measurement of three $2P \rightarrow 2S$ transitions in μd [4]. This value is 2.7 times more accurate but 7.5σ smaller than the CODATA-2010 value. It is also 3.5σ smaller than the r_d obtained just from electronic deuterium spectroscopy [10].

Clearly, these results indicate that there is a "*deuteron radius puzzle*" in addition to the already known "*proton radius puzzle*".

2.4 Summary

There is a clear discrepancy in the proton and deuteron rms charge radii obtained from electronic vs muonic atoms. The uncertainties in the electron scattering results are too large to have an impact on helping resolve the discrepancy. Therefore, there is an urgent need for an electron scattering experiment which can extract the deuteron radius more precisely than achieved to date. We propose an experiment which can accomplish the higher precision by using a single setup to measure e-d and e-p scattering and use a pure QED cross section such as the Møller scattering cross section for normalization rather than the e-p scattering cross section as have been done for all previous electron scattering experiments. This experiment will also extract the deuteron radius via two complementary methods; a) by extracting the charge form factor from e-d scattering cross sections normalized to Møller scattering and b) by extracting the deuteron structure radius from the ratio of e-d to e-p scattering. The ability to extract the deuteron charge radius using two complementary methods will help reduce the systematic uncertainties.

The recently completed PRad experiment, has successfully demonstrated the techniques proposed in this experiment. The PRad experiment was able to reach the lowest Q^2 of any electron scattering experiment, and at the same time cover a wide range in Q in a single setting, to enable a precise extrapolation to $Q^2 = 0$. Using an upgraded version of the PRad setup we can measure e-d, e-p and Møller scattering in the same experimental setup. This will allow us to extract the most precise deuteron charge radius to date using electron scattering and thereby make a direct impact on the "*deuteron radius puzzle*".

3 Overview of the Proposed Measurement

The PRad collaboration at JLab developed and successfully ran a new magnetic-spectrometer-free, calorimetric experiment to measure the proton charge radius with a high precision. This method has a proven ability to reach extreme small scattering angles ($\theta_e = 0.7^\circ - 6.0^\circ$), as well as measure a well known QED process, $e^-e^- \rightarrow e^-e^-$ Møller scattering in parallel to the main process, to control the systematic uncertainties (see Sec. 4 for details).

We propose to perform a new electron scattering experiment on deuterium ($ed \rightarrow ed$) at small angles to address the newly developed *"deuteron charge radius puzzle"* in hadronic physics. As in the case of the $ep \rightarrow ep$ experiments, most of the $ed \rightarrow ed$ experiments quoted in literature have been performed with a traditional magnetic spectrometer method. Almost all of them implemented the detection of the recoiled deuterons to control the elasticity in the scattering process.

Similar to the PRad experiment, the proposed $ed \rightarrow ed$ scattering experiment will use the HyCal calorimeter together with an additional cylindrical Si-strip recoil detector. The proposed experimental apparatus will include:

(1) a windowless gas flow deuterium/hydrogen target;

(2) cylindrical Si-strip detector for detection of the recoiling low-energy deuterons;

(3) two planes high position resolution GEM detectors to provide tracking of the scattered electrons and dramatically improve the Q^2 resolutions;

(4) scintillator veto counters in front of the HyCal calorimeter to provide time of flight information on the scattered electrons;

(5) high resolution and high acceptance PrimEx HyCal calorimeter located at $\sim$ 5.7 m downstream from the gas target to measure scattered electrons energies and positions (see Sec. 5).

The proposed experimental design will allow the detection of the scattered electrons to angles as low as $\sim 0.7^{\circ}$ and recoiling deuteron nuclei to ensure the elasticity in the measured cross sections. Also, with its high acceptance and azimuthal symmetry, the setup will simultaneously detect multi-electron processes such as Møller scattering, for the first time in $ed \rightarrow ed$ scattering experiments.

3.1 Major advantage of the proposed experiment

This experiment will have three major improvements over previous $ed \rightarrow ed$scattering experiments:

(1) The cross sections will be normalized to the well known QED process - Møller scattering, which will be measured simultaneously during the experiment within similar detector acceptances. This, arguably, will be a superior method to control the systematic uncertainties in the $ed \rightarrow ed$ cross sections.

(2) The proposed non-magnetic and calorimetric experiment will have the ability to reach extreme forward angles for the first time in ed scattering experiments. The experimental setup will cover the very forward angles $(0.7^{\circ} - 6^{\circ})$, which in turn will allow for access to extremely low Q^2 range ($\sim$ $(2 \times 10^{-4}$ - $5 \times 10^{-2})$ $(\mathrm{GeV/c})^2)$ for few GeV incident electron beams. The lowest Q^2 range measured in ed scattering to date is from Ref. [21], where the minimum value of Q^2 reached is $2 \cdot 10^{-3}$ $(\mathrm{GeV/c})^2$. The very low Q^2 range is critically important since the rms charge radius of the deuteron is being extracted as the slope of the measured deuteron charge form factor, $G_{Cd}(Q^2)$ at the Q^2=0 point (see Eq. 3). We also understand that in going to very small Q^2 range, one has to take care of the uncertainties in the measured cross sections and Q^2, as well as, still provide a reasonably large interval of Q^2 to facilitate the extraction of the slope from G_{Cd} *vs.* Q^2 dependence.

In order to achieve these objectives we propose to run at two different beam energies, which will ensure coverage of a large enough range in Q^2 and also provide significant overlap in the Q^2 range for systematic studies. This will also help control the systematics of the radiative correction calculations. Moreover, the large range in Q^2 will be covered in a single setting without any change to the experimental setup, unlike in magnetic spectrometer experiments. This last point is a significant advantage over previous measurements.

(3) We propose to use a windowless gas flow target in this experiment. This will sufficiently cut down the experimental background from the target windows which is typical for most of the previous $ed \rightarrow ed$ experiments. With this type of gas target the majority of events detected in the setup will be produced by the two processes: $ed \rightarrow ed$ and $e^-e^- \rightarrow e^-e^-$, both of which are of direct interest in this proposed experiment. The electro-disintegration of the target deuterons ($ed \rightarrow epn$ inelastic breakup reaction) will constitute the major part of the background in this experiment. The suggested measurements of the time-of-flight (between the veto counters and the recoil detector) and the azimuthal angles (between GEMs and recoil detector) will effectively control this background (Sec. 7.2).

As stated above, the proposed experimental setup will allow for a direct and simultaneous detection of both $ed \rightarrow ed$ and $e^-e^- \rightarrow e^-e^-$ processes. The trigger in this experiment (total energy deposited in calorimeter $\geq 20\%$ of E_0, as described in Sec. 4.4) will allow for the effective detection of the Møller events in both single-arm and double-arm modes. In the case of double-arm mode, already two selection criteria, the co-planarity and elasticity in energy (described in Sec. 6.2.2) will provide a good event selection in this rather low background experiment.

3.2 Normalization to the Møller cross section

The $ed \to ed$ elastic cross sections in this proposed experiment will be normalized to the $e^-e^- \to e^-e^-$ Møller cross sections, which can be calculated with a sub-percent accuracy within the QED framework, including the radiative corrections.

The experimental differential cross sections for $ed \to ed$ scattering can be written as:

$$\left(\frac{d\sigma}{d\Omega}\right)_{ed}(Q_i^2) = \frac{N_{\rm exp}^{\rm yield}\,(ed \to ed \text{ in } \theta_i \pm \Delta\theta)}{N_{\rm beam}^{e^-} \cdot N_{\rm tgt}^{\rm D} \cdot \varepsilon_{\rm geom}^{ed}\,(\theta_i \pm \Delta\theta) \cdot \varepsilon_{\rm det}^{ed}}\,. \tag{8}$$

On the other hand, the differential cross sections for the Møller process, measured simultaneously in this experiment, will have a similar dependence on the experimental quantities:

$$\left(\frac{d\sigma}{d\Omega}\right)_{e^-e^-} = \frac{N_{\rm exp}^{\rm yield}\,(e^-e^- \to e^-e^-)}{N_{\rm beam}^{e^-} \cdot N_{\rm tgt}^{\rm D} \cdot \varepsilon_{\rm geom}^{e^-e^-} \cdot \varepsilon_{\rm det}^{e^-e^-}}\,, \tag{9}$$

where $N_{\rm exp}^{\rm yield}\ (ed \to ed \text{ in } \theta_i \pm \Delta\theta)$ is the number of elastically scattered $ed \to ed$ events inside a particular azimuthally symmetric ring on GEM/HyCal with polar angles in $(\theta_i \pm \Delta\theta)$ range which defines the $Q_i^2 \pm \Delta Q^2$ for a fixed incident energy (see Fig. 2); $N_{\rm exp}^{\rm yield}\,(e^-e^- \to e^-e^-)$ is the same quantity as for ed, defined in three different ways described below; $N_{\rm beam}^{e^-}$ is the number of beam electrons that passed through the target with the number of D atoms/cm^2 - $N_{\rm tgt}^{\rm D}$, during the measurement; $\varepsilon_{\rm geom}^{ed}\,(\theta_i \pm \Delta\theta)$ is the geometrical acceptance of the $(\theta_i \pm \Delta\theta)$ ring for the $ed \to ed$ reaction; $\varepsilon_{\rm geom}^{e^-e^-}$ is the same for the $e^-e^- \to e^-e^-$ process and it will be calculated in three different ways depending on the accepted method for the Møller process, and it is described below; $\varepsilon_{\rm det}^{ed}$ and $\varepsilon_{\rm det}^{e^-e^-}$ are the detection efficiencies of the particular elements of the setup for the scattered electrons

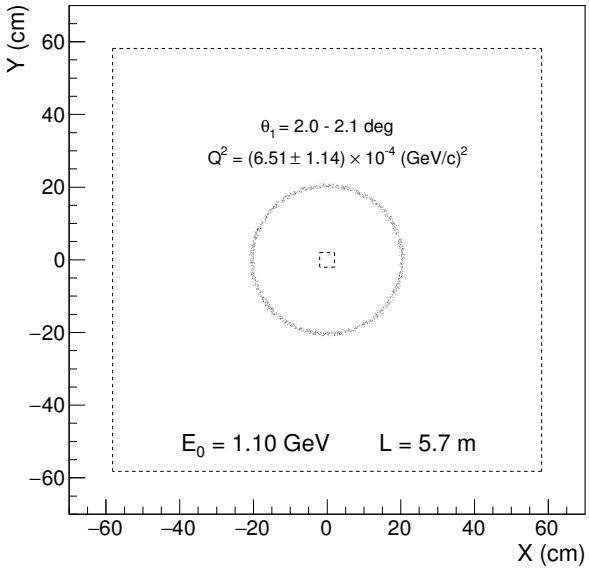

Figure 2: The simulated $X-Y$ position distribution of a single Møller scattered electron in the calorimeter at $E_0 = 1.1$ GeV. The angular range of the detected electron is $\theta_1 = 2.0^\circ - 2.1^\circ$ giving a Q^2 range of $Q^2 = (6.5 \pm 1.1) \cdot 10^{-4}\ ({\rm GeV/c})^2$.

The ratio of Eqs. 8 to 9 will relate the ed cross sections relative to the e^-e^- Møller cross sections, as:

$$\left(\frac{d\sigma}{d\Omega}\right)_{ed}(Q_i^2) = \left[\frac{N_{\rm exp}^{\rm yield}\left(ed \to ed \text{ in } \theta_i \pm \Delta\theta\right)}{N_{\rm exp}^{\rm yield}\left(e^-e^- \to e^-e^-\right)} \cdot \frac{\varepsilon_{\rm geom}^{e^-e^-}}{\varepsilon_{\rm geom}^{ed}} \cdot \frac{\varepsilon_{\rm det}^{e^-e^-}}{\varepsilon_{\rm det}^{ed}}\right] \left(\frac{d\sigma}{d\Omega}\right)_{e^-e^-} . \tag{10}$$

Right away, the two major sources of systematic uncertainties, $N_{\rm beam}^{e}$ and $N_{\rm tgt}^{\rm H}$, in the above ratio which dominated in the previous experiments are simply canceling out in this proposed experiment.

The remaining two sources of systematic uncertainties: the ratio of the geometrical uncertainties $\left(\varepsilon_{\rm geom}^{e^-e^-}/\varepsilon_{\rm geom}^{ed}\right)$ and the detection efficiency $\left(\varepsilon_{\rm det}^{e^-e^-}/\varepsilon_{\rm det}^{ed}\right)$ will have a different impact on the final systematic uncertainties depending on the selection method of the Møller events. Both scattered electrons from the Møller process will be detected by GEM and HyCal, as in the previous PRad experiment. However, the requirement to detect the recoiling deuteron nucleus will introduce a sizable asymmetry in both detection efficiency $\varepsilon_{\rm det}^{ed}$ and geometrical acceptance $\varepsilon_{\rm geom}^{ed}$ of the $ed \to ed$ reaction *vs.* Møller. Therefore, these quantities will have contributions from the recoil detector which we plan to determine experimentally during the calibration runs.

3.3 Calibration of the recoil detector

Both detection efficiency $\varepsilon_{\rm det}^{ed}$ and geometrical acceptance $\varepsilon_{\rm geom}^{ed}$ of the recoil detector will be measured during special runs with hydrogen gas in the windowless target maintained at the same pressure as the deuterium gas during the production run. The kinematics of the $ep \to ep$ scattering is very similar to the $ed \to ed$ elastic scattering process at these very forward scattering angles. In both cases the proton and deuteron are recoiling with a similar polar angles, very close to 90° (see Figs. 3 and 4).

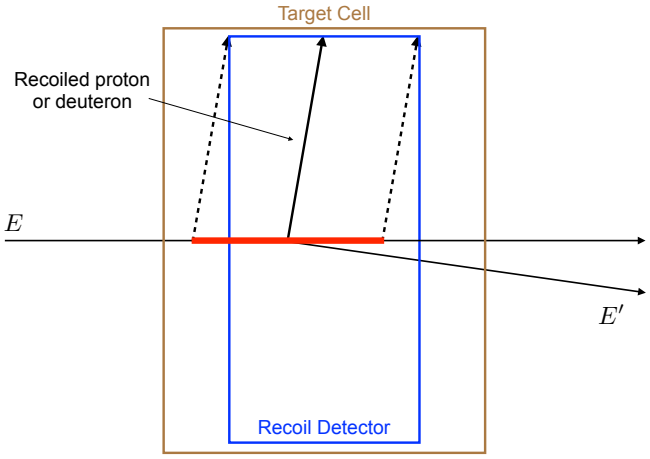

Figure 3: Schematic of the z-acceptance for the $ep \to ep$ and $ed \to ed$ elastic scattering processes.

Fig. 5 shows the similarity of the simulated z-acceptance for both $ep \to ep$ and $ed \to ed$ elastic scattering processes in our setup for a slice of electron scattering angles around 2° at 1.1 GeV beam energy. The active length of the Si-strip detectors is selected to be shorter than the effective and relatively uniform part of the gas flow target in order to include similar target length for both scattering processes and for each scattering angle. The simulated density profile of hydrogen gas in the target cell is shown in Fig. 6, the density profile for deuterium should be identical.

During the recoil detector calibration run we plan to accumulate experimental data for the $ep \to ep$, and simultaneously for the $e^-e^- \to e^-e^-$, with high statistics (similar to the main $ed \to ed$ process, $\sim 0.2\%$ per Q^2 bin). That will allow us to extract a similar ratio as in the Eq. 10, only for the hydrogen target:

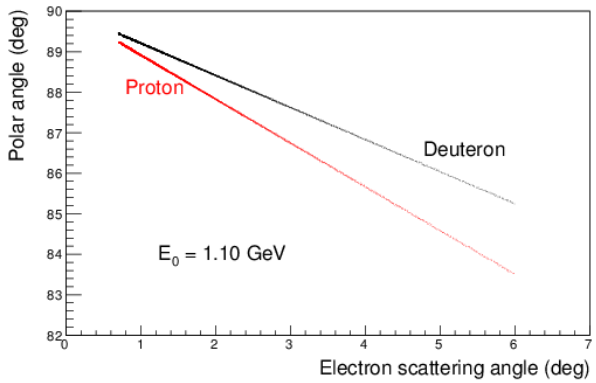

Figure 4: The simulated distribution of the deuteron (black) and proton (red) polar angle *vs.* electron scattering angle for the $ep \to ep$ and $ed \to ed$ elastic scattering processes at $E_0 = 1.1$ GeV.

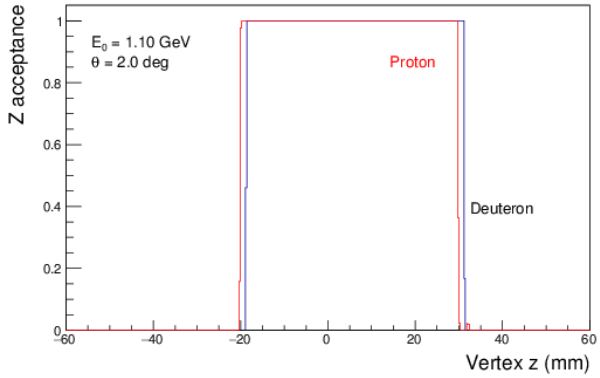

Figure 5: The z-vertex acceptance for $ed \to ed$ and $ep \to ep$ for a slice of electron scattering angles around 2° at $E_0 = 1.1$ GeV.

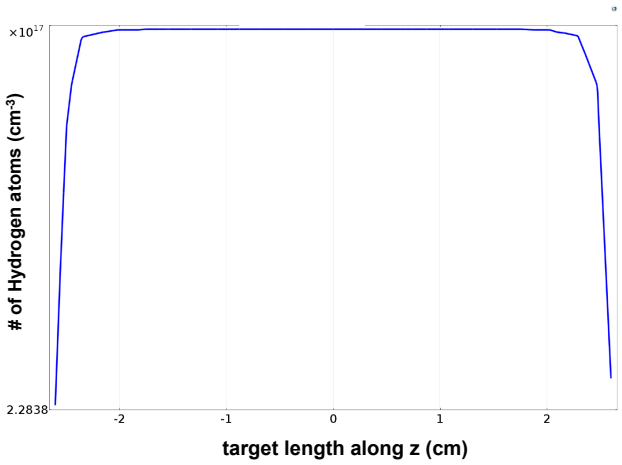

Figure 6: The simulated density distribution along the z-direction for hydrogen gas injected into the target cell (done using the COMSOL package).

$$\left(\frac{d\sigma}{d\Omega}\right)_{ep}(Q_i^2) = \left[\frac{N_{\rm exp}^{\rm yield}\left(ep \to ep \text{ in } \theta_i \pm \Delta\theta\right)}{N_{\rm exp}^{\rm yield}\left(e^-e^- \to e^-e^-\right)} \cdot \frac{\varepsilon_{\rm geom}^{e^-e^-}}{\varepsilon_{\rm geom}^{ep}} \cdot \frac{\varepsilon_{\rm det}^{e^-e^-}}{\varepsilon_{\rm det}^{ep}}\right] \left(\frac{d\sigma}{d\Omega}\right)_{e^-e^-}. \tag{11}$$

The ratio of the geometric acceptances $\left(\varepsilon^{e^-e^-}_{\rm geom}/\varepsilon^{ed}_{\rm geom}\right)$ and the detection efficiencies $\left(\varepsilon^{e^-e^-}_{\rm det}/\varepsilon^{ed}_{\rm det}\right)$ needed for the cross section in Eq. 10 can be measured by using the differential cross sections, $\left(\frac{d\sigma}{d\Omega}\right)_{ep}$, measured in the PRad experiment with a high precision.

3.4 Møller event selection methods

We are planning to use three different approaches for the identification of the Møller events to reduce systematics in precise determination of the Møller scattering process.

3.4.1 Single-arm Møller event selection method

The proposed experimental setup (see Sec. 5) is optimized such that both Møller scattered electrons will be detected in the GEM/HyCal for angles $\geq 0.7^\circ$ (see Sec. 6.2.2. However, looking at Eq. 10 for the case when one defines the Møller process inside the same angular $(\theta_i \pm \Delta\theta)$ ring (see Fig. 2) with one of the scattered electrons detected (single-arm Møller method), then we get $\varepsilon^{ed}_{\rm geom} = \varepsilon^{e^-e^-}_{\rm geom}$ and $\varepsilon^{ed}_{\rm det} = \varepsilon^{e^-e^-}_{\rm det}$ having in mind the different energy values of these electrons. With that, Eq. 10 becomes:

$$\left(\frac{d\sigma}{d\Omega}\right)_{ed}(Q^2_i) = \left[\frac{N^{\rm yield}_{\rm exp}\left(ed \to ed \text{ in } \theta_i \pm \Delta\theta\right)}{N^{\rm yield}_{\rm exp}\left(e^-e^- \to e^-e^-\right)}\right]\left(\frac{d\sigma}{d\Omega}\right)_{e^-e^-} \tag{12}$$

and, therefore, allows for a determination of the ed scattering cross sections essentially without systematic uncertainties related to the experimental apparatus.

Since the $e^-e^- \to e^-e^-$ is a two-body reaction, the experimental scattering angle of one of the electrons, together with the well known incident beam energy $(\Delta E/E = 10^{-4})$), will define the kinematics of the process. With that, the measured energy in the calorimeter $(E_{\rm meas})$ can be used to select the events in the experiment. Figure 7 demonstrates the the energy resolution of the calorimeter is sufficient for a high level of confidence that this selection criterion alone will allow for an effective selection of events in this low-background experiment. Figure 8 also demonstrates the effective separation of Møller events from the ed elastic scattered events for angles $\theta_e > 0.7^\circ$, planned for this experiment. The Møller event generator includes radiative effects, developed for the PRad experiment [36]. The radiative corrections for the $ed \to ed$ process are being developed based on the formalism for $ep \to ep$ that was implemented for the PRad experiment.

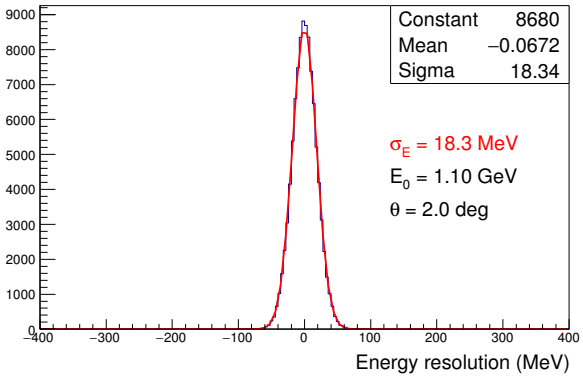

Figure 7: The simulated energy resolution for detecting a single Møller scattered electron in the calorimeter at $E_0 = 1.1$ GeV and $\theta_e = 2^\circ$. The value of the resolution was obtained from the PRad experiment.

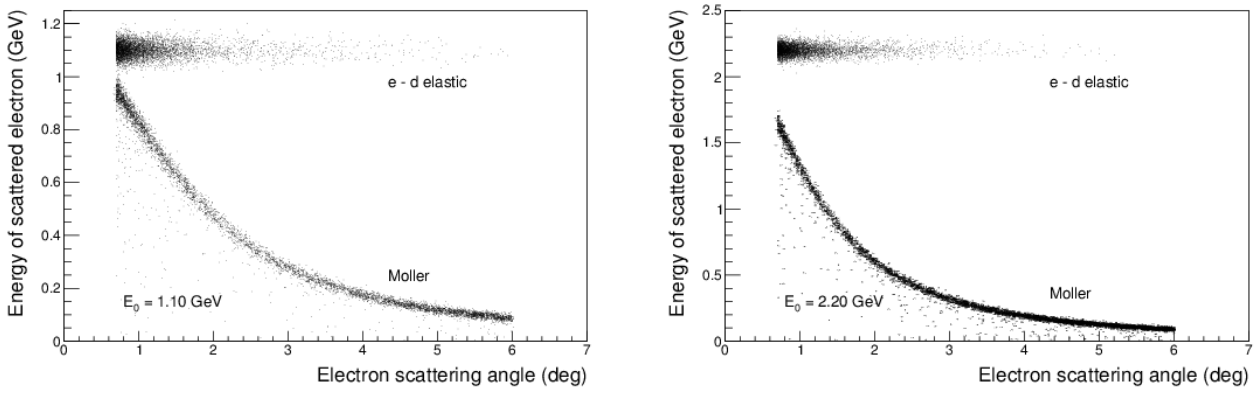

Figure 8: The simulated energy *vs.* scattering angle distribution of $e-d$ elastic and one of the Møller scattered electrons at $E_0 = 1.1$ GeV (left) and at $E_0 = 2.2$ GeV (right). The Møller event generator includes radiative effects, developed for the PRad experiment.

3.4.2 Coincident event selection method

As already mentioned above, the proposed experiment is optimized in a way that both electrons from $e^-e^- \rightarrow e^-e^-$ will be detected in the calorimeter for angles $\theta_e > 0.7^\circ$. We will also explore the selection of Møller events in coincidence. As illustrated in Fig. 9, this method, in addition to the same Q_i^2 ring $(\theta_i \pm \Delta\theta)$, will introduce a second ring on the calorimeter for the detection of the second Møller scattered electron. As a consequence, it may introduce different geometrical acceptances and detection efficiencies for the particular Q^2. It can be calculated by Monte Carlo simulations and tested by the extracted Møller cross sections.

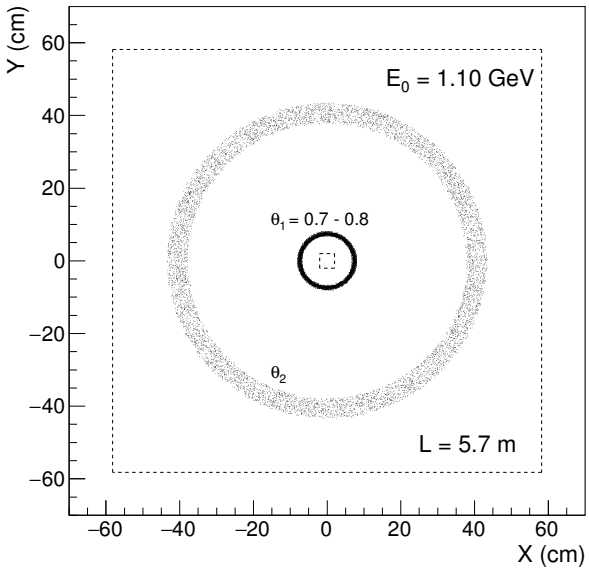

Figure 9: The simulated $X-Y$ position distribution of the two Møller scattered electrons on the HyCal calorimeter at a distance of ~ 5.7 m from the target at an incident beam energy of 1.1 GeV. The distribution of the second electron is shown as the outer ring θ_2 when the first electron is in the range $\theta_1 = 0.7^\circ - 0.8^\circ$. The outside square box is the size of the HyCal calorimeter.

3.4.3 Integrated Møller cross section method

In this case, we will normalize the ed cross sections to the Møller cross sections extracted from the entire fiducial volume of the calorimeter for all Q^2 values. With that, Eq. 10 becomes:

$$\left(\frac{d\sigma}{d\Omega}\right)_{ed}(Q_i^2) = \left[\frac{N_{\rm exp}^{\rm yield}\,(ed,\ \theta_i \pm \Delta\theta)}{N_{\rm exp}^{\rm yield}\,(e^-e^-,\ \text{on PbWO}_4)}\right] \frac{\varepsilon_{\rm geom}^{e^-e^-}(\text{all PbWO}_4)}{\varepsilon_{\rm geom}^{ed}(\theta_i \pm \Delta\theta)} \frac{\varepsilon_{\rm det}^{e^-e^-}(\text{all PbWO}_4)}{\varepsilon_{\rm det}^{ed}(\theta_i \pm \Delta\theta)} \cdot \left(\frac{d\sigma}{d\Omega}\right)_{e^-e^-}, \tag{13}$$

with $\left(\frac{d\sigma}{d\Omega}\right)_{e^-e^-}$ integrated over the HyCal/GEM acceptance.

3.5 Summary

The proposed experiment will measure the $ed \to ed$ elastic cross section with high precision over a wide range of Q^2 ($2 \times 10^{-4} \leq Q^2 \leq 5 \times 10^{-2}$ GeV^2). This experiment will reach the lowest Q^2 measured in electron scattering while at the same time covering a large range in Q^2. It will use a new calorimetric technique that allows normalization to the pure QED process of Møller scattering that is detected simultaneously with the ed elastic scattering process with the same detector acceptance. This technique was successfully demonstrated during the PRad experiment and allows excellent control over systematic uncertainties. The proposed experiment will reuse the PRad setup with two major modifications; a new cylindrical Si-strip recoil detector for ensuring elasticity and a second pair of GEM chambers to improve the vertex and Q^2 resolutions. Given the reliance on the PRad technique and setup, we will discuss some of the key features and the successes of the PRad experiment in the next section.

4 Characteristics of the PRad Experimental Setup

Last year this collaboration successfully ran the Proton Charge Radius (PRad) experiment at JLab. The PRad experiment was developed and assembled in a short few years since its full approval with "A"rating by PAC40, to measure the proton charge radius with a magnetic-spectrometer-free setup employing a high resolution and large acceptance calorimeter, that allowed for the ep scattering cross section to be normalized to the well known $e^-e^- \to e^-e^-$ Møller QED process. The PRad experiment included (1) a windowless gas flow hydrogen target used for the first time at JLab, (2) a large volume vacuum chamber with a single thin window (3) a pair of large area GEM chambers and (4) a high resolution HyCal calorimeter located about 5.6 m downstream of the target. The PRad ran during May-June 2016 utilizing a 1.1 and 2.2 GeV CW electron beam, with a width of 25μm and a position stability of better than $\pm$ 250 μm. The experiment was able to reach the lowest Q^2 (2.0×10^{-4} GeV^2) of any ep scattering experiment and at the same time covered a large range in Q^2 (2.0×10^{-4} - 5×10^{-2} GeV^2). A schematic of the experimental setup is shown in Fig. 10 and the major elements are described in the subsections below.

4.1 Windowless gas flow target

The PRad experiment in Hall B utilized a windowless, hydrogen gas flow target constructed by the Jefferson Lab Target Group, and funded by a NSF MRI grant. The windowless design of the target cell helped achieve very low backgrounds compared to previous ep scattering experiments measuring the charge radius of the proton. A schematic of the target is shown in Fig. 11. Room temperature hydrogen was flown through a 25 K heat exchanger attached to a mechanical cryocooler, and accumulated in a 80 mm diameter, 40 mm long copper target cell located within a small ($\sim$ 1 m^3) differentially pumped vacuum chamber. The target cell, which is suspended from the top of the vacuum chamber using a precision, 5-axis motion mechanism, had 7.5 μm thick kapton covers at both ends with 4 mm orifices for the electron beam to pass through the target. A schematic of the cell is shown in Fig. 11.

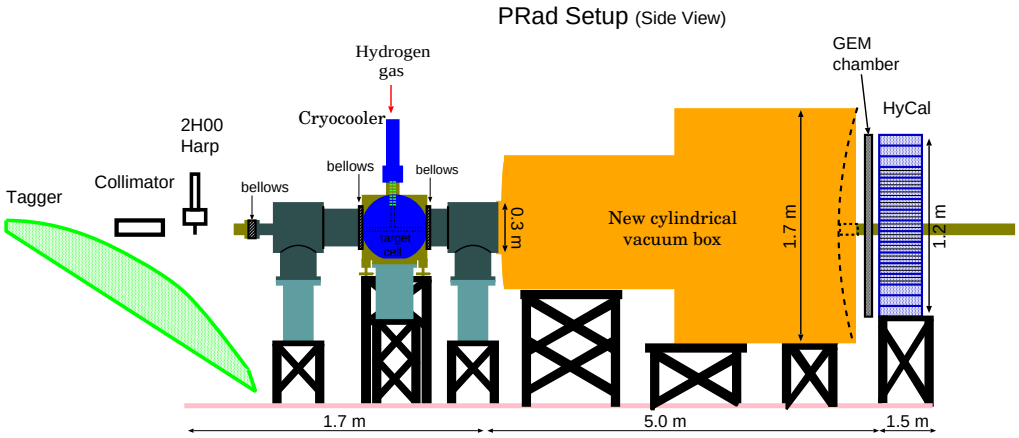

Figure 10: A schematic of the experimental setup used during the PRad experiment.

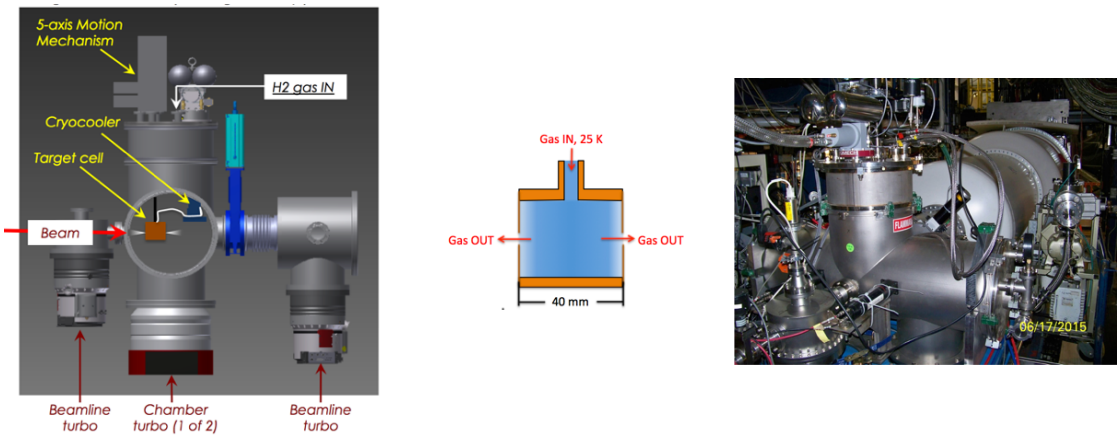

Figure 11: A schematic of windowless gas flow hydrogen target used during the PRad experiment (left). A schematic of the target cell with the 7.5 μm thick kapton covers at both ends which have a 4 mm diameter orifice for the beam to pass through (middle). A photograph of the target as it sat on the Hall-B beamline during the PRad experiment (right, please disregard the date on the photograph).

The gas was pumped out of the chamber using two large turbo molecular vacuum pumps with a combined pumping speed of 5700 l/s. The gas pressure within the cell was measured by a precision capacitance manometer and was measured to be approximately 0.5 Torr during the experiment, giving in an areal density of about 2×10^{18} H/cm^2. The pressure with gas flowing to the chamber but not the cell was $\sim$ 2 mTorr and pressure without any gas flow was 0.3 mTorr. Two additional turbo pumps were attached to the upstream and downstream ends of the vacuum chamber to maintain a beamline vacuum of less than 10^{-5} torr. Hydrogen gas was metered into the target system using a precision, room-temperature mass flow controller. A photograph of the target is shown in Fig. 11 (right).

The PRad target pressure and temperature remained stable throughout the experiment. The variation of target pressure and temperature with time is shown in Fig. 12.

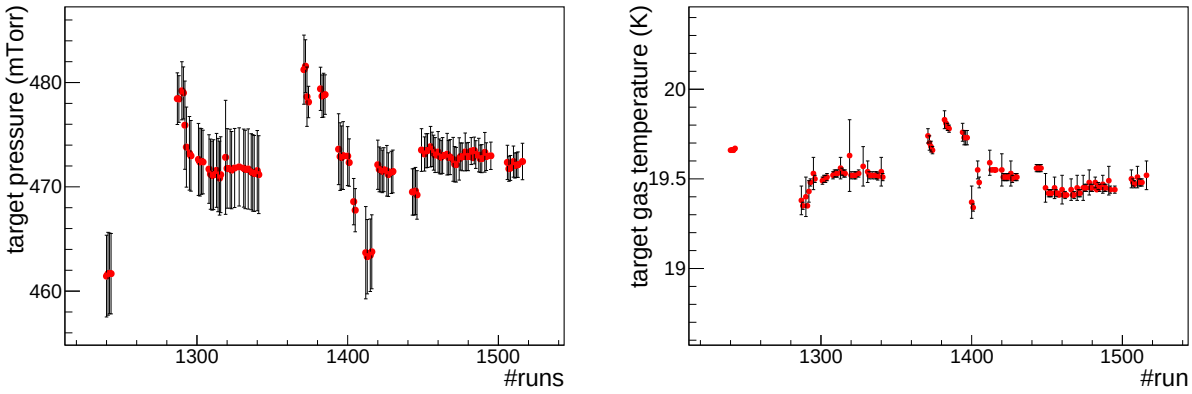

Figure 12: The variation of PRad target pressure and temeperature *vs.* run number. Each run was about 1 hr long.

4.2 Large volume vacuum chamber

For the PRad experiment a new large $\sim$5 m long, two stage vacuum chamber was designed and built. It extended from the target to the GEM/HyCal detector system. There was a single 1.7 m diameter, 63 mil thick Al. window at one end of the vacuum chamber, just before the GEM detector. A 2-inch diameter beam pipe was attached using a compression fitting to the center of the thin window. This design ensured that the electron beam did not encounter any additional material other than the hydrogen gas in the target cell, all the way down to the Hall-B beam dump. The vacuum box also helped minimize multiple scattering of the scattered electrons en route to the detectors. A photograph of the vacuum chamber is shown in Fig. 13.

4.3 GEM detectors

The PRad experiment used Gas Electron Multiplier (GEM) based coordinate detectors, they consisted of a pair of large area 1.2 m$\times$ 0.6 m three layer ionization chambers, with $\sim$ 100 μm position resolution. The chambers were designed and constructed by the University of Virginia group and are currently the largest such chambers to be used in a nuclear physics experiment. These GEM chambers provided more than a factor of 20 improvement in coordinate resolution and a similar improvement in the Q^2 resolution. They allowed unbiased coordinate reconstruction of hits on the calorimeter, including the transition region of the HyCal calorimeter. The GEM detectors also allowed us to use the lower resolution Pb-glass part of the calorimeter, extending the total Q^2 range covered at a single beam energy setting.

The chambers were mounted to the front face of the HyCal calorimeter using a custom mounting frame. Each chambers had a 2-inch hole to allow the beam pipe to pass through the chambers. A pre-mixed gas of 70% Argon and 30% CO_2 was continuously supplied to the chambers. Photographs of the GEM detectors is shown in Fig. 14.

The PRad GEM detectors were read out using the APV25 chip based Scalable Readout System (SRS) developed at CERN by the RD51 collaboration. The APV25 chip samples 128 channels in parallel at 20 MHz or 40 MHz and stores 192 analog samples, each covering 50 ns or 25 ns, per channel. Following a trigger, up to 30 consecutive samples from the buffer are read-out and transmitted to an ADC unit that de-multiplexes the data from the 128 channels and digitizes the analog information.

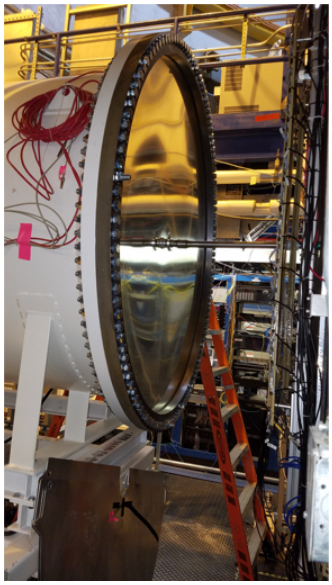

Figure 13: A photograph of the ∼5 m long, two stage vacuum chamber used during the PRad experiment (left, please disregard the date on the photograph). A photograph of the 1.7 m diameter thin window at one end of the vacuum chamber (right). Here the GEM and HyCal have been moved downstream for technical service.

The SRS system consists of the following components:

- SRS-APV25 hybrid cards mounted on the detector. These cards contain the 128 channel APV25 chip which reads data from the detector, multiplexes the data, and transmits analog to the ADC card via standard commercial HDMI cables.
- SRS-ADC unit that houses the ADC chips that de-multiplex data and convert into digital format.
- SRS-FEC card which handles the clock and trigger synchronization. A single Front End Card (FEC) and ADC card combination has the capability to read data from up to 16 APV hybrid cards. The data from the FEC are send either directly to the data acquisition computer (DAQ PC) or to the SRS-SRU via a 10 Gb/sec fiber link.
- SRS-SRU, Scalable Readout Unit, handles communication between multiple (up to 40) FEC cards and the data acquisition computer. It also distributes the clock and trigger synchronization to the FEC cards.
- The data acquisition computer was used as a readout controller and as a part of the larger PRad-DAQ system.

A total of 9216 electronics channels are needed to readout the PRad GEM chambers. This amounts to 72 SRS-APV25 cards (128 channels per card). The SRS-ADC / SRS-FEC card can handle up to 16 SRS-APV25 cards and send data to the SRS-SRU through a newly implemented 10Gb Fiber link. We use

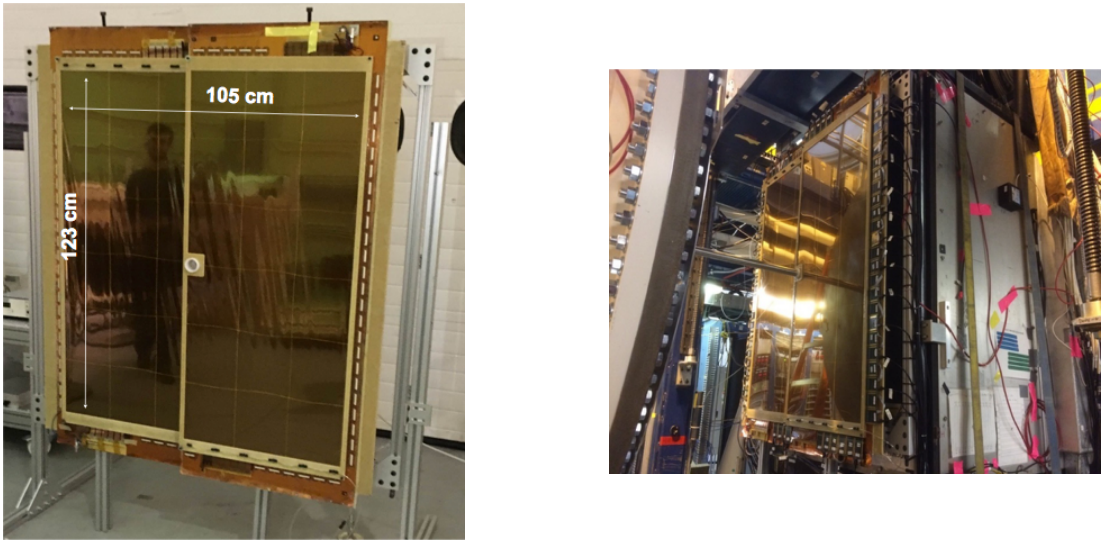

Figure 14: A GEM based coordinate detector used in the PRad experiment (left). A photograph of the GEM chambers mounted to the front of the HyCal calorimeter (right). Here the GEM and HyCal have been moved downstream for technical service.

6 SRS-ADC/SRS-FEC cards to read out all 72 SRS-APV25 cards limiting the number of SRS-APV25 card per SRS-FEC to 12. The SRS-FECs cards are connected to 2 SRS-SRU boards (3 SRS-FECs per SRS-SRU). An upgraded firmware allowed the experiment to collect data at $\sim$ 5kHz with a data rate of $\sim$ 400 MB/sec and $\sim$ 90% live time. This was the highest DAQ rate achieved by a APV based system. A schematic of the GEM DAQ system is shown in Fig. 15.

The PRad GEM based coordinate detector consistently performed well throughout the experiment. The efficiency of the chamber was uniform over the entire chamber as shown in Fig. 16, and it achieved the design resolution of 72 μm, as shown in Fig. 27. The performance of the detector remained stable throughout the experiment.

4.4 HyCal electromagnetic calorimeter

The PrimEx Collaboration at JLab, using a previous MRI award constructed a novel state-of-the-art multi-channel electromagnetic hybrid ($PbWO_4$-lead glass) calorimeter (HyCal) [37] to perform a high precision measurement of the neutral pion lifetime via the Primakoff effect [38]. The PRad experiment used the high resolution and large acceptance PrimeEx HyCal electromagnetic calorimeter to detect the scattered electrons from ep and Møller scatterings with high precision.

A single $PbWO_4$ module is 2.05×2.05 cm^2 in cross sectional area and 18.0 cm in length ($20X_0$). The crystal part of the calorimeter consists of 1152 modules arranged in a 34×34 square matrix (70×70 cm^2 in size) with four crystal detectors removed from the central part (4.1×4.1 cm^2 in size) for passage of the incident electron beam. The scintillation light from the electromagnetic shower in the crystals was detected with Hamamatsu R4125HA photomultiplier tubes (PMT) coupled at the back of the crystals with

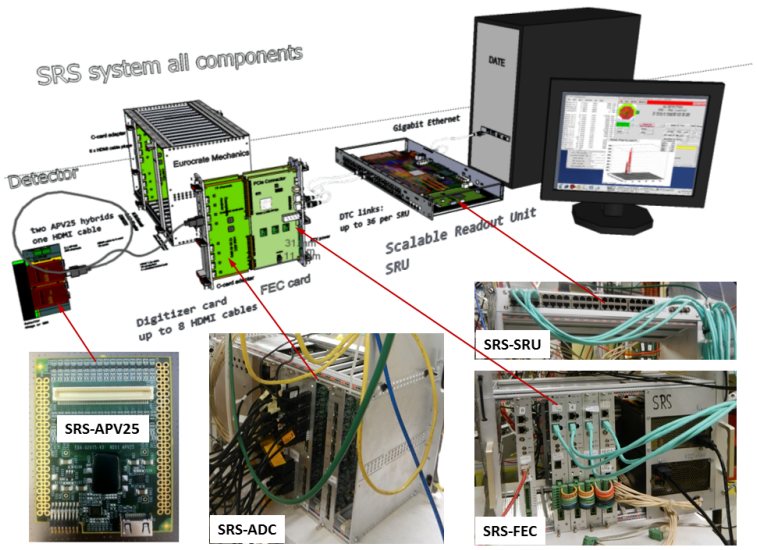

Figure 15: A schematic of the PRad GEM DAQ system.

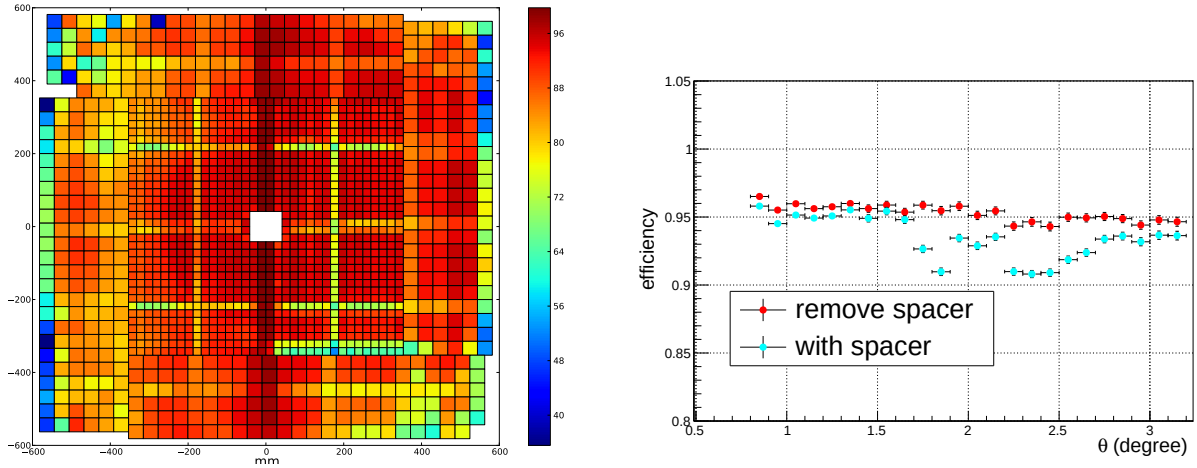

Figure 16: A plot of the GEM efficiency over the X-Y coordinates of the detector (left), and the GEM efficiency over the region overlapping with the $PbWO_4$ crystals of the HyCal calorimeter *vs.* polar angle (right). The drops in efficiency seen in the 2D plot in the left is due to spacers inside the GEM modules. A software cut to remove the spacers yields an efficiency profile uniform to within +/- 1% level as seen by red circles. The cut to remove spacers reduce the available statistics by only about 4.7%.

optical grease. Each module is supplied with high voltage and is equipped with readout of dynode and anode signals. Each crystal was first wrapped in $\sim$ 63 μm VM-2000 reflector (from 3M company), then with a 38.1 μm black Tedlar for optical isolation between the blocks. The PMT housings were attached to the crystals with two specially designed brass flanges on the front and back of the crystals, stretched with two 25 μm brass strips. In addition, a LED based light monitoring system is used to deliver a pulse of light to each module via a fiber optic cable. Figure 17 shows the assembled PrimEx HyCal calorimeter before the final installation of the gain monitoring system. The calorimeter will be located at a distance of about 5.7 m from the target which will provide a geometrical acceptance of about 25 msr.

The energy calibration of HyCal was performed by continuously irradiating the calorimeter with the Hall

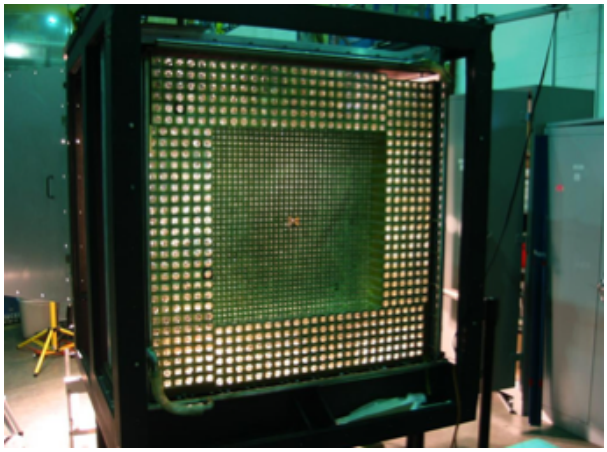

Figure 17: The PrimEx HyCal calorimeter which was developed by the PrimEx collaboration using a previous MRI award shown with all modules of the high performance $PbWO_4$ crystals in place and before installation of the gain monitoring system in front of the calorimeter.

B tagged photon beam at low intensity (< 100 pA). An excellent energy resolution of $\sigma_E/E = 2.6\%/\sqrt{E}$ has been achieved by using a Gaussian fit of the line-shape obtained from the 6×6 array. After subtraction of the beam energy spread due to the finite size of the scintillating fiber, as well as multiple scattering effects in vacuum windows and in air, a level of 1.2% energy resolution was reached for 4 GeV electrons. The impact coordinates of the electrons and photons incident on the crystal array were determined from the energy deposition of the electromagnetic shower in several neighboring counters. Taking into account the photon beam spot size at the calorimeter (σ=3.0 mm), the overall position resolution reached was $\sigma_{x,y} = 2.5\ \mathrm{mm}/\sqrt{E}$ for the crystal part of the calorimeter. The calorimeter performed as designed during the experiment, as shown in Fig. 18, which shows the resolution achieved during the PRad experiment and the energy dependence of the trigger efficiency.

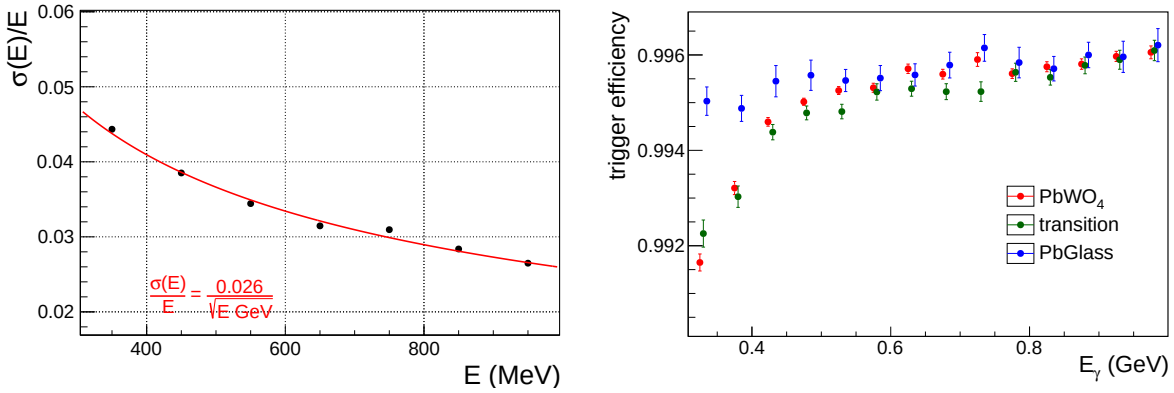

Figure 18: Energy resolution of the $PbWO_4$ crystal part of the HyCal calorimeter (left) and the energy dependence of the trigger efficiency (right). These data are from the PRad experiment.

As the light yield of the crystal is highly temperature dependent ($\sim$ 2%/°C at room temperature), a special frame was developed and constructed to maintain constant temperature inside of the calorimeter with a high temperature stability (± 0.1°C) during the experiments. The trigger in this experiment (total energy deposited in the calorimeter $\geq$ 20% of E_0) allowed for the detection of the Møller events in both single-arm and double-arm modes.

4.5 Summary

The PRad experiment successfully demonstrated the technique of magnetic spectrometer free measurement of ep scattering at small angles using a windowless gas flow target, A GEM detector and a high resolution calorimeter. This technique let the PRad experiment achieve the lowest Q^2 (2.0×10^{-4} GeV^2) of any ep scattering experiment and at the same time cover large range in Q^2 (10^{-4} - 6×10^{-2} GeV^2), as shown in Fig. 19. It also demonstrated the effectiveness of using the simultaneous detection of Møller and elastic scattering to reduce the systematic uncertainties.

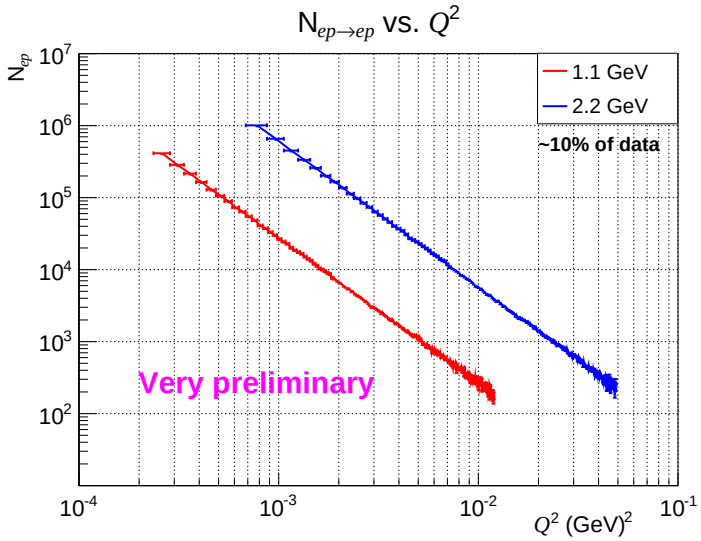

Figure 19: The range in Q^2 covered during the PRad experiment as shown by the number of ep events collected at a beam energy of 1.1 and 2.2 GeV. Only a small fraction of the full statistics is shown here.

5 Proposed Experimental Setup

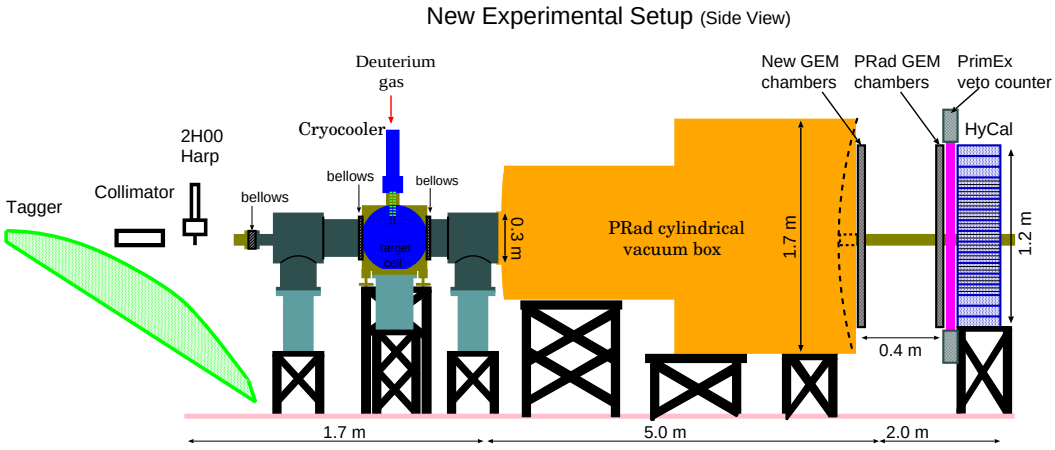

Figure 20: A schematic of the setup for the proposed experiment.

The proposed experiment will reuse the PRad setup with two major changes to adapt it for measuring

elastic ed scattering. It will use the PRad windowless gas flow target, with a new target cell redesigned to hold a cylindrical Si-strip recoil detector inside the cell. The large volume vacuum chamber with a single thin window will be reused and the high resolution HyCal calorimeter, along with the GEM chamber plane attached to the front of it will also be reused. A second plane of GEM chamber will be added such that the two plane of chambers are ∼40 cm apart. The PrimEx scintillator veto counter will be added in front of the HyCal. A schematic of the experimental setup is shown in Fig. 20 and the unique elements are described in the subsections below.

5.1 Electron beam

We propose to use the CEBAF beam at two incident beam energies $E_0 = 1.1$ and 2.2 GeV for this experiment. The beam requirements are listed in Table 1. All of these requirements were achieved during the PRad experiment. A typical beam profile during the PRad experiment is shown in Fig. 21 and the beam X, Y position stability of $\simeq \pm 0.1$ mm is shown in Fig. 22.

Table 1: Beam parameters for the proposed experiment

Energy (GeV)	current (nA)	polarization (%)	size (mm)	position stability (mm)	beam halo
1.1	1 - 20	Non	< 0.1	≤ 0.2	$\sim 10^{-7}$
2.2	1 - 20	Non	< 0.1	≤ 0.2	$\sim 10^{-7}$

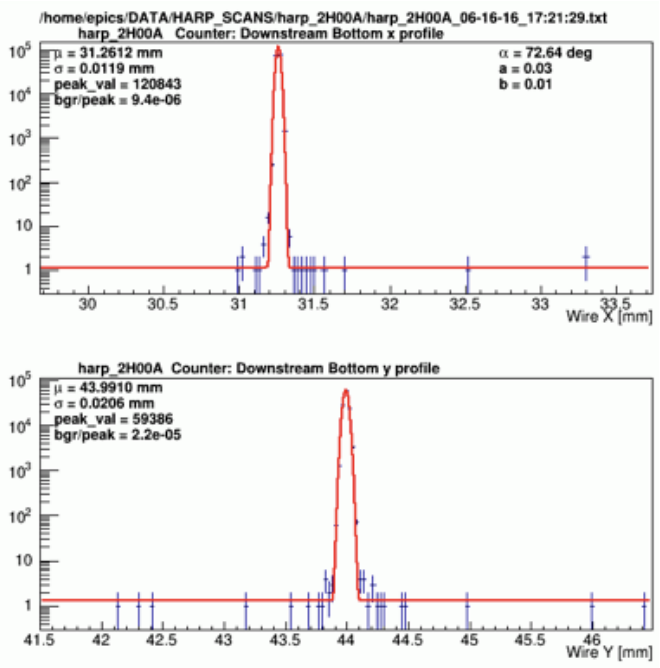

Figure 21: Typical beam profile during the PRad experiment, showing a beam size of $\sigma_x = 0.01$ mm and $\sigma_y = 0.02$ mm.

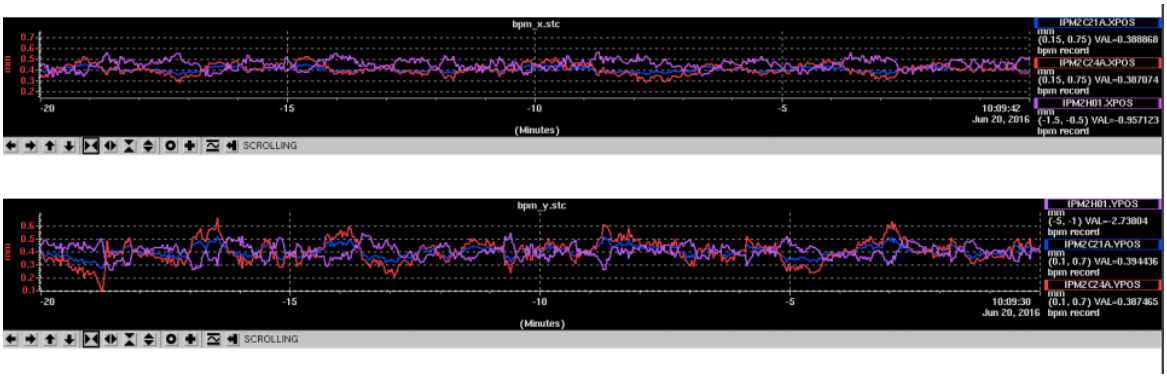

Figure 22: Beam X,Y position stability ($\simeq \pm$ 0.1 mm) during the PRad experiment.

5.2 Windowless gas flow target

We will use the windowless gas flow target developed for the PRad experiment. A new target cell will be built such that it can accommodate the Si-strip recoil detector inside it. The target cell will be made out copper and will have dimensions of 30×30×5.5 cm^3. It will have thin (7 μm) Kapton foils on the sides facing the beam with a 4 mm aperture in the center for the beam to pass through. The front and back faces of the target cell will have 20 feedthroughs for the readout electronics of the Si-strip detector as shown in Fig. 24. The gas inlet is also modified compared to the cell used in the PRad experiment. It will inject the gas from the top edge of the front and back faces rather than from the top of the cell. Room temperature deuterium gas will be flown through a 25 K heat exchanger attached to a mechanical cryocooler, and accumulated in the copper target cell located within a small ($<$ 1 m^3) differentially pumped vacuum chamber. The target cell will be suspended from the top of the vacuum chamber using a precision, 5-axis motion mechanism. The gas will be pumped out of the chamber using two large turbo molecular vacuum pumps with a combined pumping speed of 5700 l/s. The gas pressure within the cell will be measured by a precision capacitance manometer and is expected to be approximately 0.5 torr during the experiment, giving in an areal density of about 2×10^{18} D/cm^2. Two additional turbo pumps attached to the upstream and downstream ends of the vacuum chamber will help maintain a beamline vacuum of less than 10^{-5} torr. The gas will be metered into the target system using a precision, room-temperature mass flow controller.

5.3 Cylindrical recoil detector

The design of the recoil detector is based on the CLAS12 Barrel Silicon Tracker (BST) [39, 40]. We will enclosed a cylindrical recoil detector within the target cell. It will consist of 20 panels of twin single sided silicon strip detectors. Each panel will be 52 mm long and 42 mm wide arranged as a do-decagon, as shown in Fig. 23 and 24. Each panel will consist of a thin, 200 μm sensor and a thick, 300 μm sensor. Each sensor will consist of 256 strips with linearly varying angles of 0° - 3°. This graded angle design minimizes dead zones. The strips will have a constant ϕ pitch of $\sim$ 200 μm ($\sim$1/85°). Fig. 25 shows the strips on the thin inner sensor and the thick outer sensor and also the intersection pattern. This detector will have angular resolution of $\delta\phi \leq$ 5 mrad and $\delta\theta \leq$ 10-20 mrad.

In order to minimize multiple scattering, essential for low momentum tracking, the materials budget will be reduced to $<$1% radiation length. The sensors will be mounted on a composite backing structure consisting of Rohacell 71 core , bus cable and a carbon fiber skin made from K132C2U fibers oriented in a quasi-isotropic pattern. The bus cable is made from a Kapton sheet with 3μm thick copper traces, which are 0.5 mm wide that provide the high voltage to the sensor on one side while the other side forms the grounding

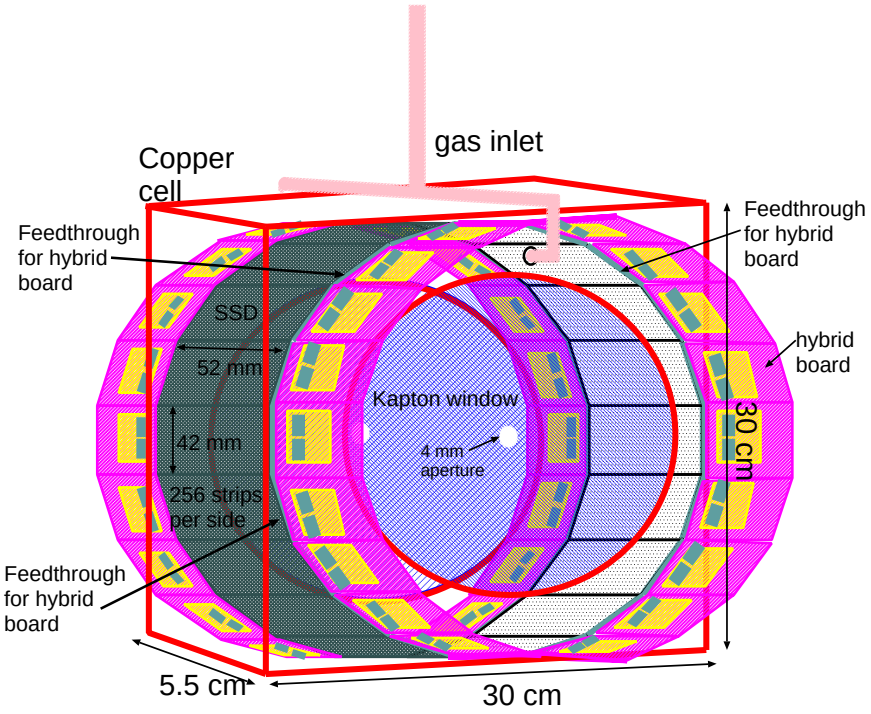

Figure 23: A schematic of the cylindrical recoil detector consisting of 20 silicon strip detector modules, held inside the target cell. All solids are shown as transparent for ease of viewing.

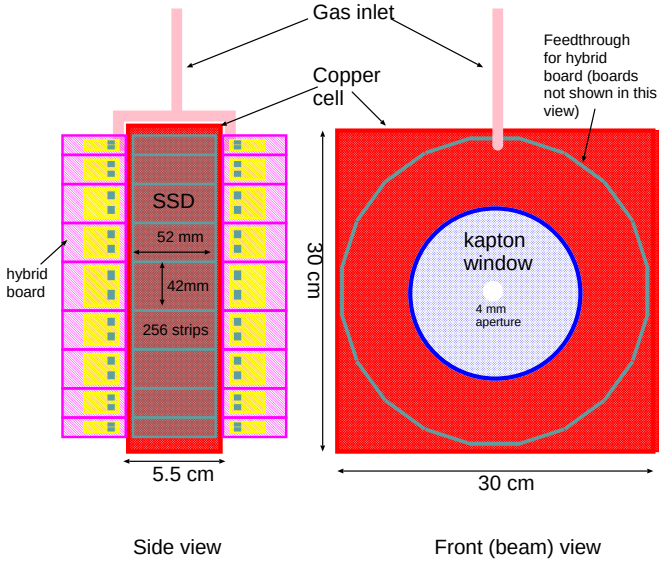

Figure 24: The front and side views of the recoil detector inside the target cell. All solids are shown as transparent for ease of viewing.

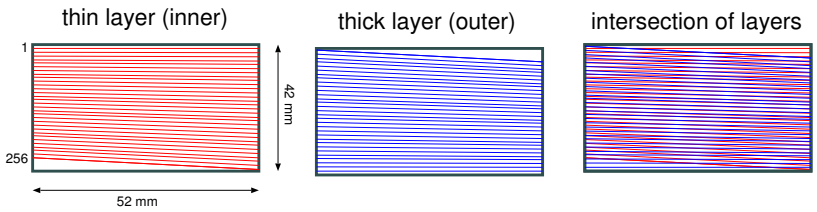

Figure 25: The layout of strips on each side of the sensors and their intersection pattern.

plane for the carbon fiber. The sensors are very similar to the ones used in the BST. The different layers of each detector module is shown in Fig. 26.

The readout system is identical to the one used by the BST in CLAS12 and we expect to use electronics from the spare planes of the BST. The readout is build on FSSR2 ASIC developed and Fermilab and fabricated by Taiwan Semiconductor Manufacturing Company. Each channel of 128 input channel of the FSSR2 chip has a preamplifier, a shaper with adjustable shaping time (50 - 125 ns), a baseline restorer, and a 3-bit ADC. The signals will be read out on the opposite side for each layer using a pitch adapter which matches the 156 μm sensor readout pitch to the 50μm bonding pad pitch of the FSSR2 chips. The signals will be read using a single rigid-flex Hybrid Flex Circuit Board (HFCB) developed at JLab for the BST. The HFCB hosts four FSSR2 chips, two on the top and two on the bottom side. Data is transferred via a flex cable to the level one connect (L1C) board. The L1C has two high density Nanonics connectors for data and control lines, Molex Micro-Fit 9-pin connector for high voltage ($\sim$ 85 V) bias to the sensors, and AMP Mini CT 17 pin connector for low voltage (2.5 V) power to the ASICs. There are 12 layers in rigid part and 6 layers in flex part. Control, data, and clock signals do not cross the ground plane splits. Clock signals are located on a separate layer. Guard traces are routed between output, clock, and power lines. Separate planes are provided for analog and digital power. To reduce noise on these planes, regulators and bypass capacitors are added. High voltage filter circuits and the bridging of high and low voltage return lines are located close to the ASICs.

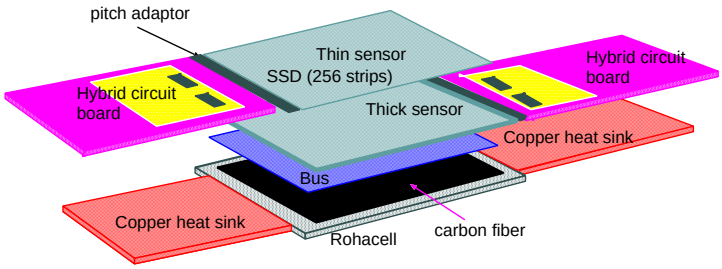

Figure 26: A schematic of the different layers of each detector module.

The period of the clock called beam crossing oscillator (BCO) sets the data acquisition time. If a hit is

detected in one of the channels, the core logic transmits pulse amplitude, channel number, and time stamp information to the data output interface. The data output interface accepts data transmitted by the core, serializes it, and transmits it to the data acquisition system. To send the 24-bit readout words one, two, four, or six Low Voltage Differential Signal (LVDS) serial data lines can be used. Both edges of the 70 MHz readout clock are used to clock data, resulting in a maximum output data rate of 840 Mb/s. The readout clock is independent of the acquisition clock. Power consumption is $\leq$ 4 mW per channel. The FSSR2 is radiation hard up to 5 Mrad.

Each of the four FSSR2 ASICs reads out 128 channels of analog signals, digitizes and transmits them to a VXS-Segment-Collector-Module (VSCM) card developed at Jefferson Lab. The event builder of the VSCM uses the BCO clock timestamp from the data word of each FSSR2 ASIC and matches it to the timestamp of the global system clock, given by the experiment trigger. The event builder buffers data received from all FSSR2 ASICs for a programmable latency time up to $\sim$ 16 μ s. The VSCM is set up to extract event data within a programmable lookback window of $\sim$ 16 μ s relative to the received trigger.

5.4 Two Planes of GEM detectors

The pair of GEM detectors used during the PRad experiment performed very well during the entire experiment yielding highly stable operation, high resolution and high efficiency, as highlighted in Fig. 27.

The experience from the PRad experiment showed that having two GEM detector layers will provide high precision track parameters for diagnostics and systematic checks of the experimental setup. Furthermore, the requirement of at least one out of two GEM layer hits for production data yields a GEM hit efficiency of close to 100% throughout the active area of the experiment; relative lateral shifting of spacers in the two GEM layers can be used to ensure uniform coverage. The two GEM layers in the proposed experiment will be separated by 40 cm. A new GEM layer (to be built) will be located next to the downstream vacuum window of the vacuum chamber. The existing GEM detector layer from pRad experiment will be located next to HyCal, 40 cm downstream of the new GEM layer. The two GEM layers will be separated by an air gap.

The new GEM layer will be designed and constructed by the University of Virginia group. This new layer will consist of two GEM modules, each having an active area of 123 cm $\times$ 55 cm, similar to the two modules the UVa group built for pRad experiment. However, the new GEM modules will be constructed using the especially thin Chromium-GEM technology currently being developed, as a result the material thickness of this new GEM layer will be approximately 0.25 $\%X_0$, about half the material thickness of a conventional GEM chamber.

In collaboration with the CERN GEM workshop, the UVa group has successfully fabricated a 10 cm $\times$ 10 cm prototype GEM chamber with Copper-less GEM foils. A conventional GEM foil consists of an insulator made of a thin Kapton foil (about 50 μm) sandwiched between two layers of copper (each about 3 μm thick). This structure is perforated with GEM holes (diameter $\sim$70 μm, pitch $\sim$140 μm). The new Copper-less GEM foils, recently developed at the CERN GEM workshop, have the copper layers of the foil removed, leaving only a 0.1 μm layer of Chromium on either side of the Kapton. The material thickness of a GEM module made of Copper-less foils is about 0.25% radiation lengths, a factor of two less than the material thickness of a conventional GEM module ($\sim$ 0.5% radiation lengths). The prototype we fabricated is the first GEM chamber to be built with Copper-less GEM foils. The initial tests of this detector indicated that it works very well delivering excellent GEM chamber performance parameters. A second generation prototype Cr-GEM detector is under testing at UVa currently. The readout of both GEM layers for the proposed experiment will be done by using the high-bandwidth optical link based MPD readout system currently being developed for the SBS program in Hall A. This new system uses the APV-25 chip used in the PRad GEM readout. However, the readout of the digitized data is performed over a high-bandwidth optical link to a Sub-System Processor (SSP) unit in a CODA DAQ setup allowing for high data volume

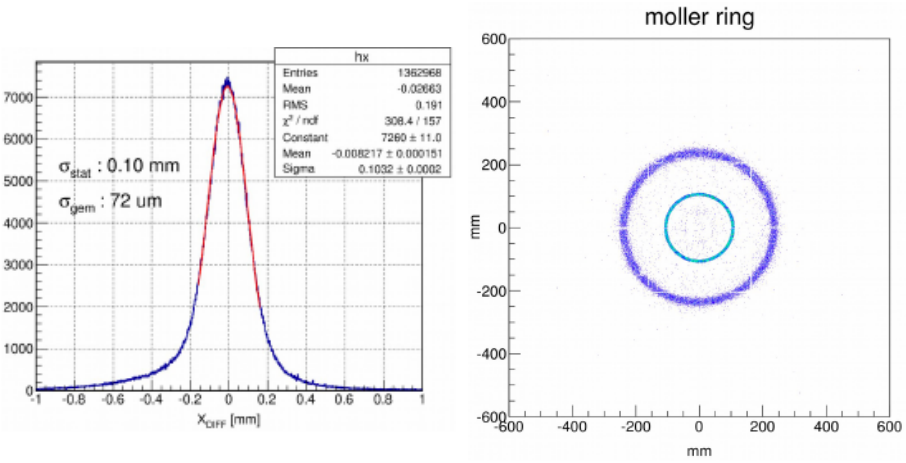

Figure 27: (Left) The position resolution (approximately 72 μm) for GEM detectors achieved during PRad experiment; this represents a factor of 20-40 improvement over the resolution available without the GEM tracker in the setup. (Right) The scattered Møller *ee* pair rings detected by PRad GEM tracker illustrating the high position resolution and accuracy provided by the GEMs. Furthermore, this plot shows the very low background level in the reconstructed GEM hit locations.

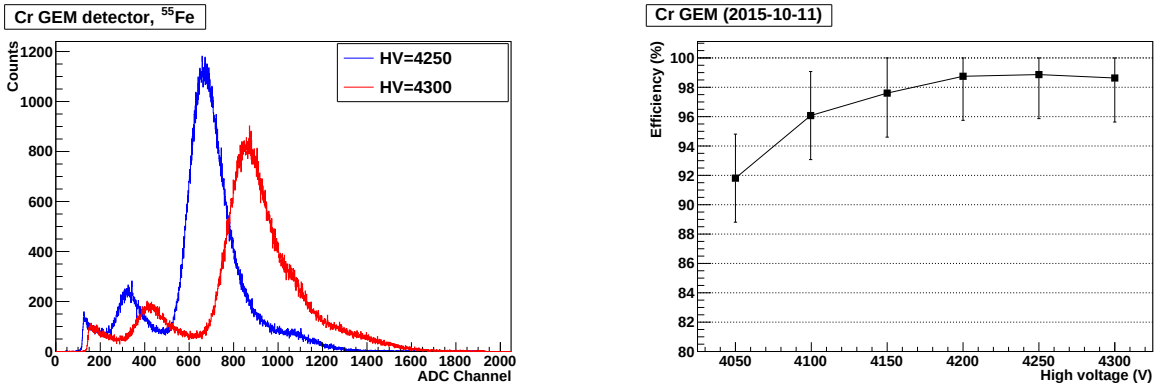

Figure 28: Characterization results for the ultra-thin Chrome-GEM module: (left) the ^{55}Fe 5.9 keV x-ray spectrum recorded by the Chrome-GEM module at two values of high voltage. The energy resolution for the 5.9 keV peak is approximately 10% (sigma), (right) the efficiency versus high voltage curve, showing the efficiency plateau. Both, the energy resolution and the efficiency plateau achieved here are similar to the values achievable from a conventional GEM module.

readout at 5 kHz. All hardware for the 160 k channel SBS readout system has already been fabricated. The optical link communication software is currently being tested. The full SBS readout system is expected to be fully operational by mid-2018. New hardware based on the same architecture will be purchased to equip the 20 k channels needed to readout the two GEM layers of the proposed experiment.

The cost of constructing the new thin GEM detector pair and a full size prototype will be approximately $ 100 k. The cost of 20 k channel of APV-25 MPD electronics system will be $ 60 k. Following the approval of this proposal, the collaboration will apply for external funds to build the new GEM layer and purchase readout electronics.

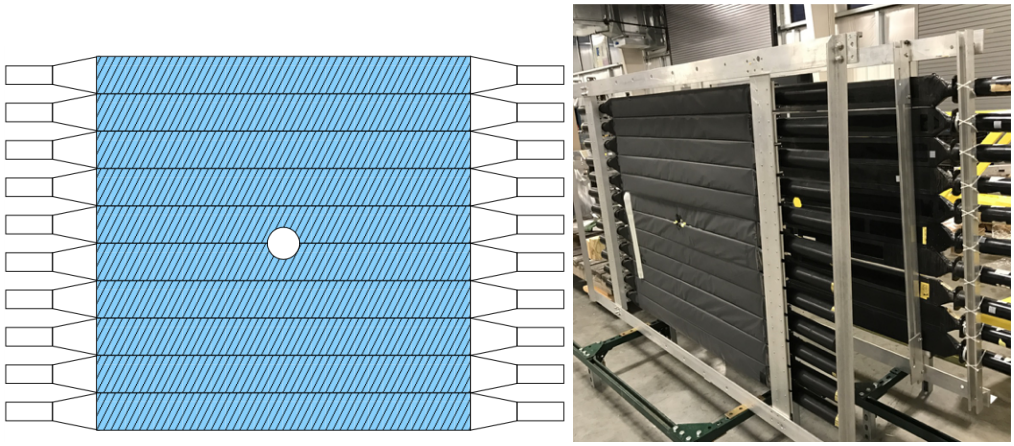

Figure 29: A schematic (left) of the X array of the veto counters and a photograph of the two arrays (right) of the veto counter.

5.5 Veto counters

To measure the time-of-flight difference between the recoil detector and the HyCal calorimeter in the experiment, an array of scintillator paddles from the PrimEx setup (used as neutral particle veto in PrimEx) will be used in front of the HyCal calorimeter. A schematic (left) of the array and a photograph of the two arrays (right) is shown in Fig. 29. The ten scintillators paddles with PMT on both ends will cover the full solid angle spanned by the calorimeter. The time-of-flight difference between the Hall-B tagger and the veto counters as measured during the PrimEx experiment is shown in Fig. 30. This plot is obtained by integrating over all Pb-glass blocks of the HyCal calorimeter. The second smaller peak is from secondary charge particles in the shower (so called albedo effect). The resolution of the first peak is $\sim$ 0.7 ns. In the proposed experiment the GEM detectors will provide high resolution hit position information which should allow time-of-flight resolution of 0.5 ns We have assumed a conservative estimate of 1 ns in our simulations described in Sec. 6.

5.6 HyCal calorimeter

The PrimEx HyCal high resolution and large acceptance electromagnetic calorimeter will be used in this experiment. It will be used to detect the scattered electrons from ed elastic and Møller scattering with high precision.

As described previously in Sec. 4.4, a single $PbWO_4$ module is 2.05×2.05 cm^2 in cross sectional area and 18.0 cm in length ($20X_0$). The crystal part of the calorimeter consists of 1152 modules arranged in a 34×34 square matrix (70×70 cm^2 in size) with four crystal detectors removed from the central part (4.1×4.1 cm^2 in size) for passage of the incident electron beam. The scintillation light from the electromagnetic shower in the crystals was detected with Hamamatsu R4125HA photomultiplier tubes (PMT) coupled at the back of the crystals with optical grease. Each module is supplied with high voltage and is equipped with readout of dynode and anode signals. Each crystal was first wrapped in $\sim$ 63 μm VM-2000 reflector (from 3M company), then with a 38.1 μm black Tedlar for optical isolation between the blocks. The PMT housings were attached to the crystals with two specially designed brass flanges on the front and back of the crystals, stretched with two 25 μm brass strips. In addition, a LED based light monitoring system is used to deliver a pulse of light to each module via a fiber optic cable. The calorimeter will be located at a distance of about 5.5 m from the target which will provide a geometrical acceptance of about 25 msr. The energy

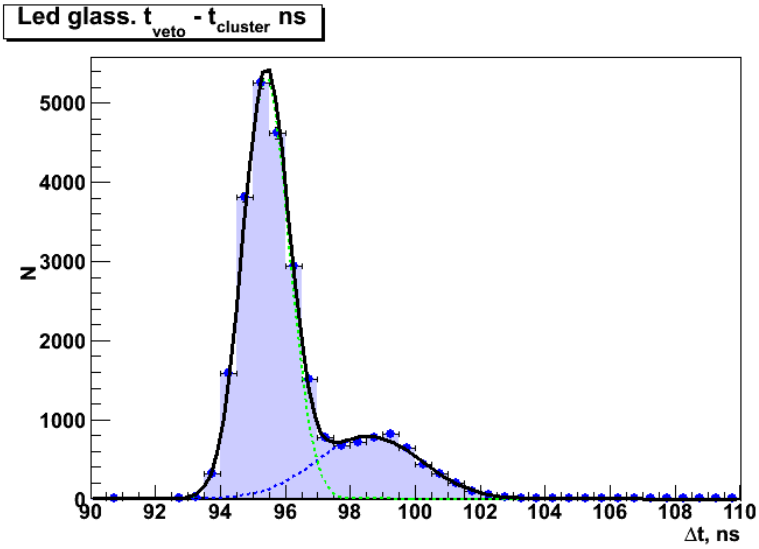

Figure 30: The time-of-flight difference between the Hall-B tagger and the veto counters integrated over all Pb-glass blocks of the HyCal calorimeter. The second smaller peak is from secondary charge particles in the shower (so called albedo effect).

calibration of HyCal will be performed by continuously irradiating the calorimeter with the Hall B tagged photon beam at lowest intensity.

As the light yield of the crystal is highly temperature dependent ($\sim$ 2%/°C at room temperature), a special frame was developed and constructed to maintain constant temperature inside of the calorimeter with a high temperature stability (± 0.1°C) during the experiments.

5.7 Electronics and Trigger

The readout electronics and DAQ for the first pair of GEM chambers and HyCal calorimeter will be exactly same as what was used during the PRad experiment. For the recoil detector readout electronics we plan to use the electronics borrowed from the spare Hall-B SVT detector plane as discussed in Sec. 5.3. The electronics for the new plane of GEM chamber will have to be procured as discussed in Sec. 5.4.

The trigger in this experiment will be set to the total energy deposited in the calorimeter $\geq 20\%$ of E_0. This will allow for the detection of the Møller events in both single-arm and double-arm modes.

We estimate (see Sec. 8) the $ed \to ed$ rate to be about 200 Hz, the Møller rate to be about 400 Hz and the deuteron electro-disintegration rate to be about 500 Hz. This give a total physics trigger rate of $\sim$1.1 kHz. Given that the energy threshold for the calorimeter will be set to $\geq 20\%$ of E_0, the total trigger rate for the proposed experiment is expected to be at the level of 4 kHz. The PRad DAQ was easily able to handle rates up to $\sim$ 5 kHz and hence the exptected rate is well within the capabilities of the DAQ.

6 Kinematics and Experimental Resolutions

6.1 Kinematics

Two main processes considered in this proposal, $ed \to ed$ scattering and Møller scattering $e^-e^- \to e^-e^-$ are both two-body reactions. Therefore, a minimum of two kinematical variables are required for the kinematical reconstruction of the reaction. Measuring more than two variables in the experiment will allow to select elastic events from competing physics processes and accidental background.

In this experiment the energy and momentum of the incident electron beam are known with high precision ($\Delta E/E \sim 10^{-4}$, emittance $\epsilon \sim 10^{-3}$ mm-mrad). Since the deuteron is a rather loosely bound nucleus (binding energy ~ 2.2 MeV) in order to insure the elasticity in the measured $ed \to ed$ events, in addition to detection of the scattered electron, we propose to detect the recoiling nucleus in a newly designed cylindrical recoil detector (see section 5.3). Just as in the PRad experiment, the energy and the (x, y) positions of the forward scattered electrons will be measured by the HyCal calorimeter and the GEM chamber attached to the front face of the calorimeter (see section 5.6 and 5.4). The scintillator veto counters just in front of the calorimeter (see section 5.5) will fix the arrival time of the scattered electrons to the front of the HyCal calorimeter. We also propose to add a second GEM based position detector located 40 cm in front of the PRad GEM detector. This will allow not only to improve the position resolution of HyCal by factor of ~ 20 but, it will also significantly improve the reaction vertex reconstruction compared to the PRad experiment. The main requirement to the recoil detector is to measure the time and the azimuthal angle of elastic scattered deuteron and protons from background processes. Both scattered electrons from the Møller events will be detected in the calorimeter with measurement of the energies (E_1, E_2) and the (x, y) positions. In addition, the positions of these electrons will be measured in two GEM detectors with high precision. The incident beam energies and the range of Q^2 together with the electron scattering angle coverage are listed in table 2.

Table 2: Proposed kinematics for the deuteron charge radius measurement with the HyCal calorimeter at 5.6 m from target.

$E_{\rm beam}$ (GeV)	θ_e (deg)	Q^2 $({\rm GeV/c})^2$
1.1	0.7	$1.8 \cdot 10^{-4}$
	6.0	$1.3 \cdot 10^{-2}$
2.2	0.7	$7.2 \cdot 10^{-4}$
	6.0	$5.3 \cdot 10^{-2}$

6.1.1 Kinematics of ed scattering

Since target mass in the $ed \to ed$ elastic scattering process is much larger than the electron mass the forward scattered electron carries most part of the incident beam energy, leading to a virtual photon of only few MeVs (figure 31). For the same reason the recoiling deuteron polar angle is very close to 90 degrees with kinetic energies of a few to ten MeV scale (figures 32 and 33). To extend the Q^2 range and have some overlap between the experimental data sets we plan to run this experiment for two incident electron beam energies, $E_0 = 1.1$ and 2.2 GeV ((figure 34). The choice of calorimetric method, allows detection of smaller scattering angles, and the two incident beam energies allows coverage of a large Q^2 range (from extreme low $1.8 \cdot 10^{-4}$ to $5.3 \cdot 10^{-2}$) in a single experimental setting.

6.1.2 Kinematics of ee scattering (Møller)

As it was described earlier, we will measure the Møller scattering process on atomic electrons simultaneously with the main $ed \to ed$ elastic scattering reaction. The Møller $e^-e^- \to e^-e^-$ differential cross section, at tree level, is getting contributions from the s and t photon exchange channels. In the center-of-mass (CM) system it is given by

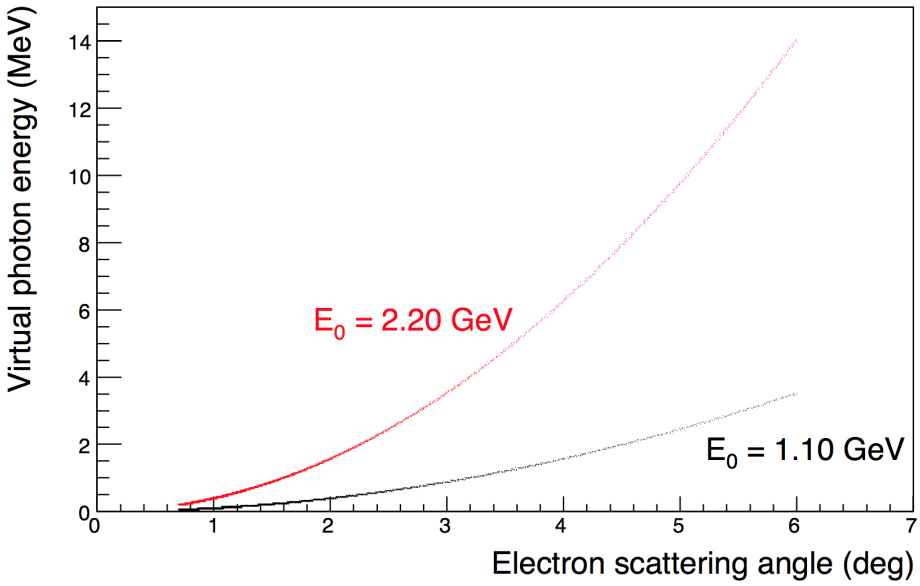

Figure 31: Virtual photon energy in $ed \to ed$ reaction *vs.* the electron scattering angle at incident beam energies of 1.1 GeV (black) and 2.2 GeV (red).

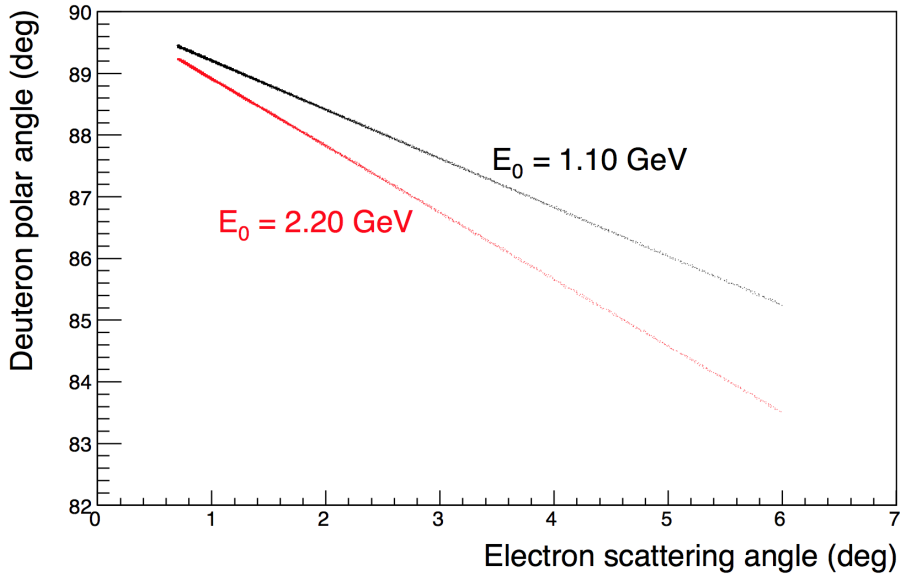

Figure 32: Recoil deuteron polar angle *vs.* the electron scattering angle at incident beam energies of 1.1 GeV (black) and 2.2 GeV (red).

$$\frac{d\sigma}{d\Omega} = \frac{\alpha^2}{s} \frac{(3+\cos^2\theta^*)^2}{\sin^4\theta^*} \tag{14}$$

for high energies where the electron mass m_e can be neglected. Here $\alpha = 1/137$ is the fine structure constant, θ^* is the CM system polar scattering angle, and s is the interaction energy squared.

Some obvious features of the Møller scattering can be deduced from Eq. 14.

- The cross section is seen to diverge at $\cos\theta^* = \pm 1$. This is due to the fact that the electron mass was

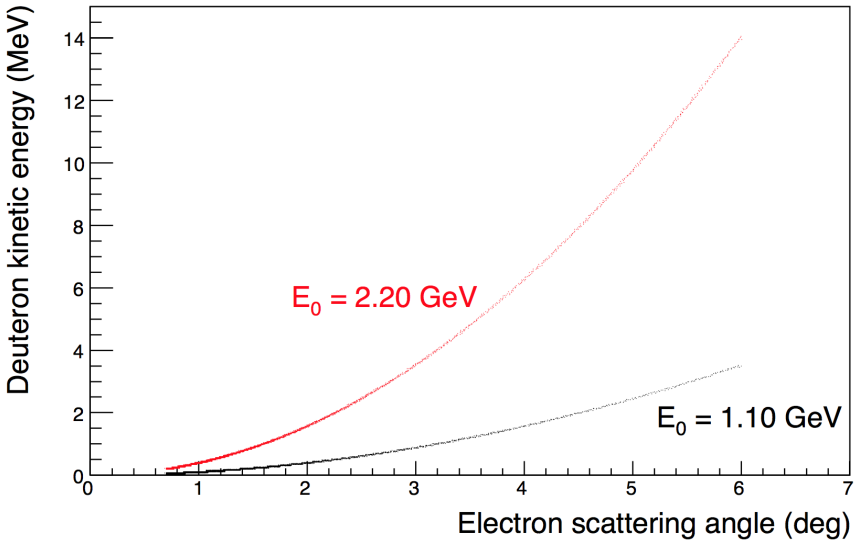

Figure 33: Recoil deuteron kinetic energy *vs.* the electron scattering angle at incident beam energies of 1.1 GeV (black) and 2.2 GeV (red).

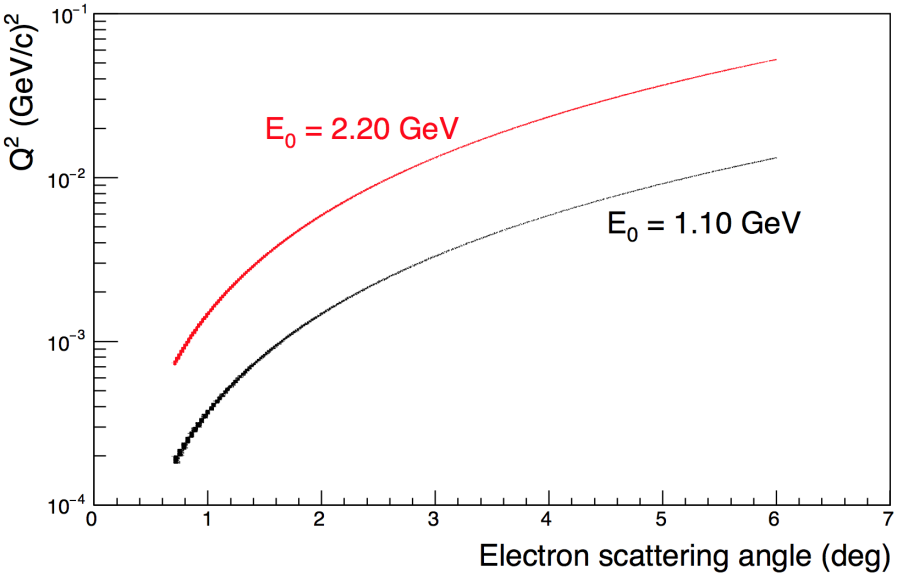

Figure 34: Four-momentum transfer squared (Q^2) in $e - d$ scattering *vs.* the electron scattering angle for both $E_0 = 1.1$ and 2.2 GeV energies.

neglected. In a rigorous treatment, where m_e is not neglected, the Møller scattering formula remains finite even at $\cos\theta^* = \pm 1$.

- The magnitude of the cross section decreases as s increases, similar to that of the e^+e^- annihilation process.

In the scattering of two electrons, s may be written in a Lorentz invariant form as

$$s = 2m_e^2 + 2m_e E_{\rm B} \,, \tag{15}$$

where $E_{\rm B}$ is the beam energy.

The laboratory momentum of the scattered electron, $p_{\rm lab}$ is given by

$$p_{\rm lab} = \gamma_{\rm CM}\sqrt{(E^* + p^*\beta_{\rm CM}\cos\theta^*)^2 - \frac{m_e^2}{\gamma_{\rm CM}^2}} \,, \tag{16}$$

where $p*$, E^* are the momentum and energy of the incident electron in the CM system and $\gamma_{\rm CM}$ is the Lorentz factor. The relation between the laboratory scattering angle $\theta_{\rm lab}$ and the CM scattering angle θ^* is given by

$$\tan\theta_{\rm lab} = \frac{1}{\gamma_{\rm CM}} \cdot \frac{\sin\theta^*}{\beta_{\rm CM}/\beta^* + \cos\theta^*} \,, \tag{17}$$

where $\beta_{\rm CM}$ is the velocity of the CM system and β^* is the velocity of the electron in the CM system.

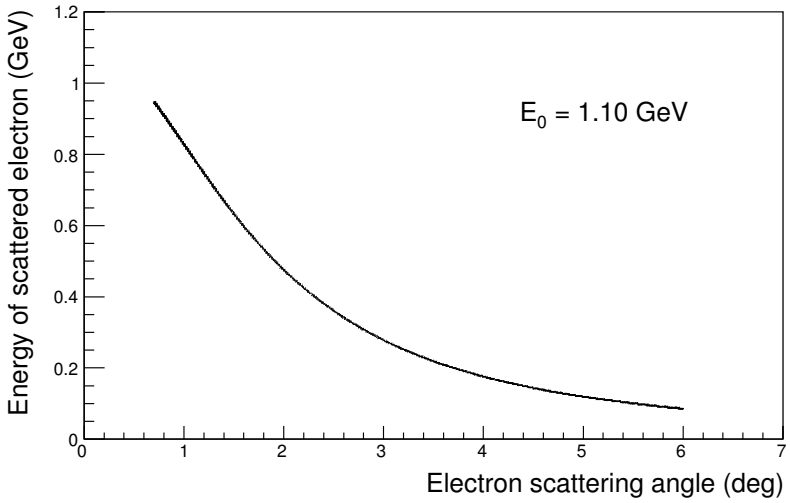

Figure 35: Energy of one of the electrons in Møller scattering *vs.* the laboratory scattering angle at an incident beam energy of 1.1 GeV.

In the CM system of the Møller scattering, the momentum and energy of the incident electron are expressed by:

$$\begin{aligned} p^* &= \sqrt{\frac{m_e(E_{\rm B} - m_e)}{2}} \quad \text{and} \\ E^* &= \sqrt{\frac{m_e(E_{\rm B} + m_e)}{2}} \,. \end{aligned} \tag{18}$$

From Eqs. 15-18 it follows that

$$p_{\rm lab} = \frac{p_{\rm B}}{2}\,(1 + \cos\theta^*) \tag{19}$$

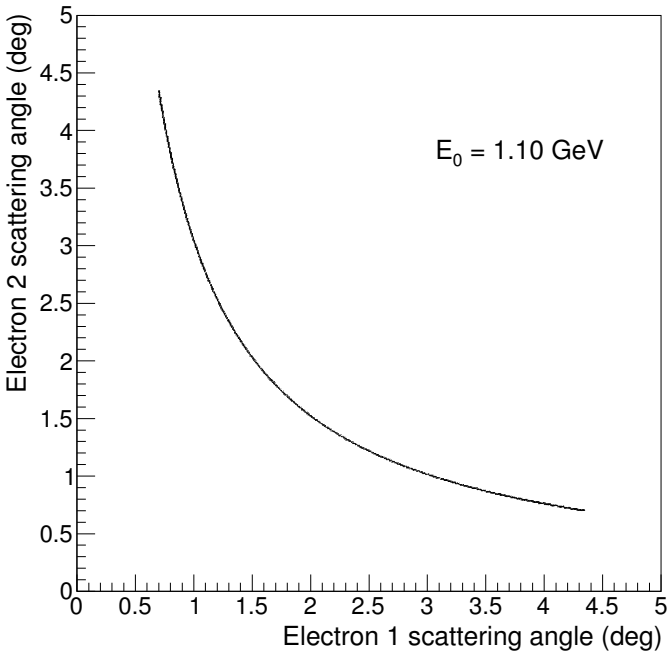

Figure 36: Angular correlation of the two electrons in Møller scattering in the laboratory system at an incident beam energy of 1.1 GeV.

so that the laboratory momentum of the scattered electron does not depend on the CM total energy, but only on the beam energy and the CM scattering angle. From Eq. 17 one obtains the expression:

$$\tan^2\theta_{\rm lab} = \frac{2m_e}{E_{\rm B}+m_e}\cdot\frac{1-\cos\theta^*}{1+\cos\theta^*}\,. \tag{20}$$

The minimum opening angle in the laboratory system between the two electrons in the Møller scattering is when $\theta^* = \pi/2$:

$$\tan^2\theta_{\rm lab} = \frac{2m_e}{E_{\rm B}+m_e}\,. \tag{21}$$

Figure 35 shows one of the Møller scattered electrons' energy *vs.* its angle. The angular correlation between the two scattered electrons in the laboratory system as a function of beam energy are shown in Figs. 36.

6.2 Experimental Resolutions

In this experiment, like in the PRad experiment, the scattered electrons from ed elastic and Møller scatterings will be detected with the high resolution, large acceptance HyCal electromagnetic calorimeter and GEM detectors.. The central part of the HyCal calorimeter ($PbWO_4$crystals) has good energy and position resolutions:

$$\begin{aligned}\sigma_E/E &= 2.6\%/\sqrt{E}\,,\\ \sigma_{x,y} &= 2.5\ {\rm mm}/\sqrt{E}\,.\end{aligned}$$

These numbers are a factor of two larger for the outside part of the calorimeter containing Pb-glass Cherenkov detectors [41].

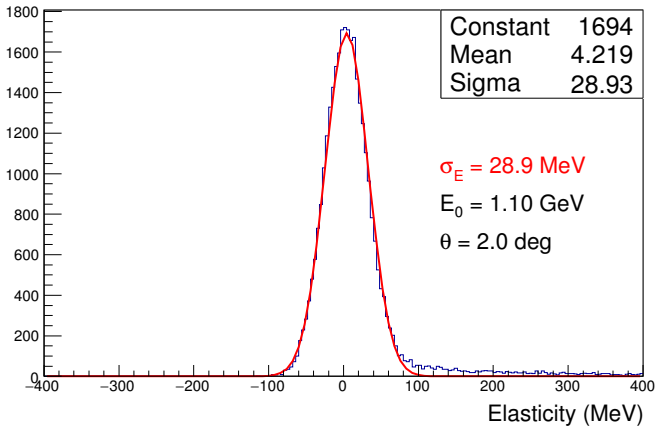

Figure 37: The *"elasticity"*, $(E_0 - E_{HyCal})$, distribution of detecting the electrons in $e-d$ elastic scattering at $E_0 = 1.1$ GeV and $\theta_e = 2^\circ$.

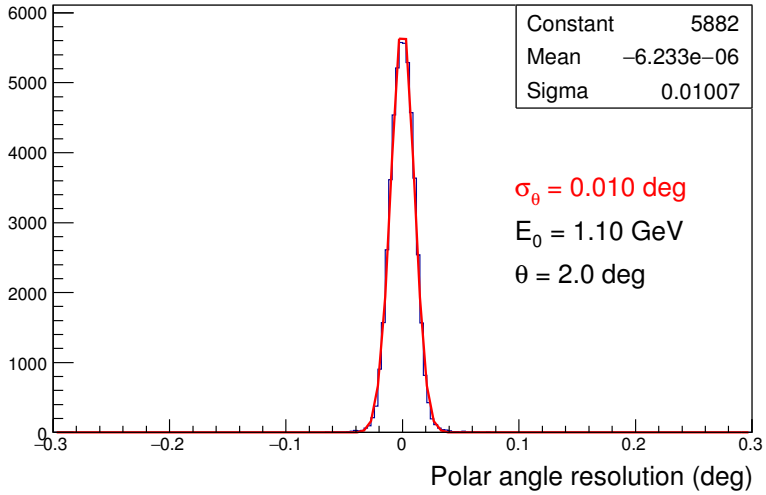

Figure 38: The polar angle resolution of detecting the scattered electrons with the GEM detectors.

In the PRad experiment we implemented one plane of GEM detectors with an excellent position resolution, ($\sim$ 72 μm) and very good electron detection efficiency ($\sim$ 93%). That dramatically improved the angular resolutions of the scattered electrons and, consequently, the resolutions in Q^2. However, the combination of one GEM and HyCal detectors did not provide a sufficient Z-vertex resolution for the effective rejection of background events from the beam line residual gas. For this experiment we are proposing to add the second GEM detector plane located at a distance of $\sim$ 40 cm from the existing PRad GEM plane. Finally, we are proposing to add a Si-strip cylindrical recoil detector in the gas flow target chamber for the detection and identification of elastic $ed \rightarrow ed$ events from the deuteron breakup background processes (Sec. 5.3)

Detailed Monte Carlo simulations based on the GEANT4 package, were carried out for ed elastic and Møller scattering. These simulations were used to study the energy and position resolutions of detecting the scattered electrons and the recoiling deuterons together with the breakup protons over the full acceptance of the experimental setup.

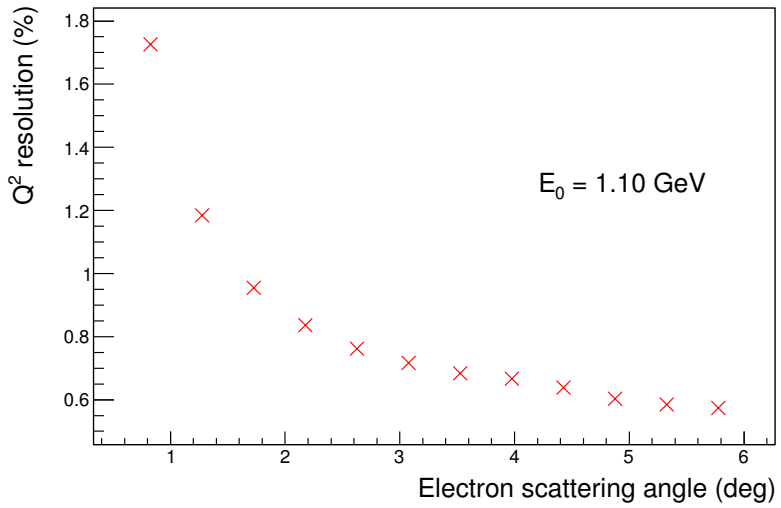

Figure 39: The Q^2 resolution for ed elastic scattering at $E_0 = 1.1$ GeV.

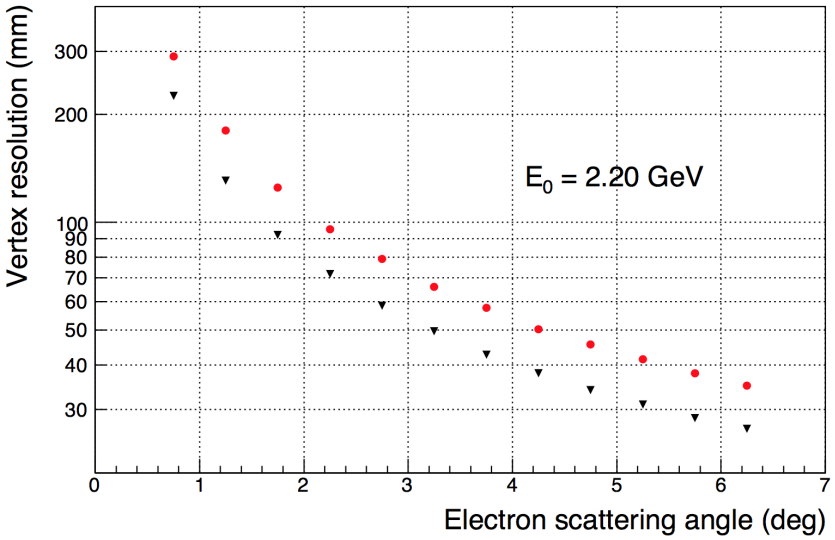

Figure 40: Vertex resolution for two different vacuum window materials, 1.6 mm Al window (used in the PRad experiment, red) and for a thinner window (0.8 mm Al, black).

6.2.1 Resolutions for the ed scattering process

Since the recoil nucleus has a kinetic energy of ~ 1 MeV at forward electron scattering angles, the difference between the incident beam energy and the detected energy in HyCal (the so called *"elasticity"*) will still be

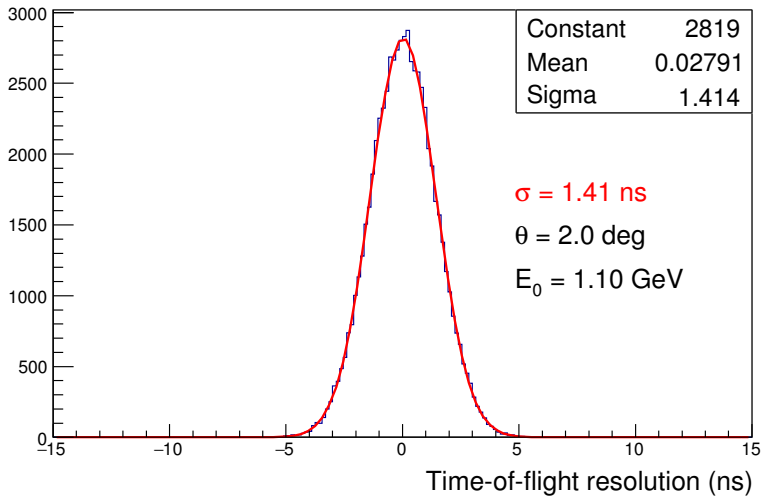

Figure 41: Time-of-flight resolution between the veto counters and the Si-strip recoil detector. The resolution is about the same for the $E_0 = 2.2$ GeV energy.

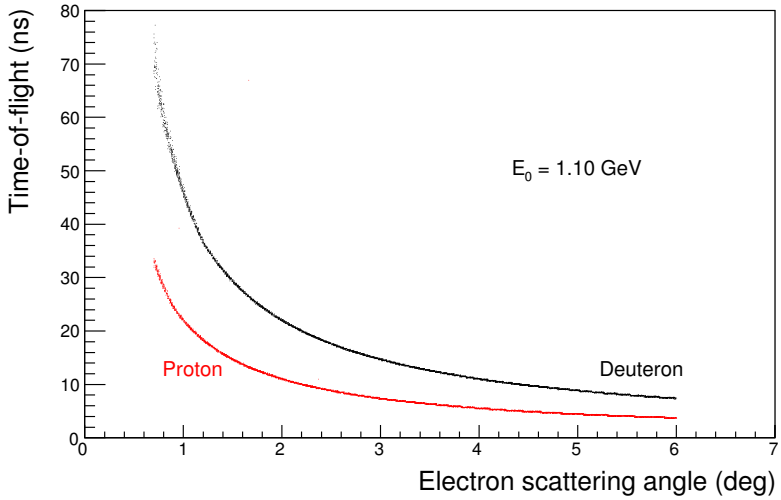

Figure 42: Time-of-flight *vs.* scattering angle for elastic $ed \to ed$ and $ep \to ep$ processes at an incident beam energy of 1.1 GeV. (ed and ep scattering are shown together for comparison only).

the first criterion in selecting the elastic events. Figure 37 shows the *"elasticity"*, $(E_0 - E_{HyCal})$, distribution in ed elastic scattering. A good energy resolution of $\sigma_E = 27$ MeV is seen at $E_0 = 1.1$ GeV.

The scattered electron polar angle will be measured by the high resolution GEM detectors (Fig. 38) providing an excellent resolution of $\sigma_{\theta_e} = 0.01^\circ$ at this forward angles. An important consideration in this type of experiments, performed at extreme forward direction, is the Q^2 resolution. Two GEM detectors, proposed in this experiment, together with the high precision of the CEBAF beam energy ($\sim 10^{-4}$), will provide a percent level resolution in Q^2 (Figure 39). The combination of two GEM detectors will also dramatically improve the reaction vertex resolution as demonstrated in Figure 40. This will allow an effective subtraction of background events from the residual gas in the upstream part of the beam line. Which is the largest background in the PRad experiment, especially at very small scattering angles.

As it is stated above, we propose to have cylindrical Si-strip sensors surrounding the gas flowing in the target area, to detect the recoiling deuterons to ensure elasticity in the ed scattering events. One of the major

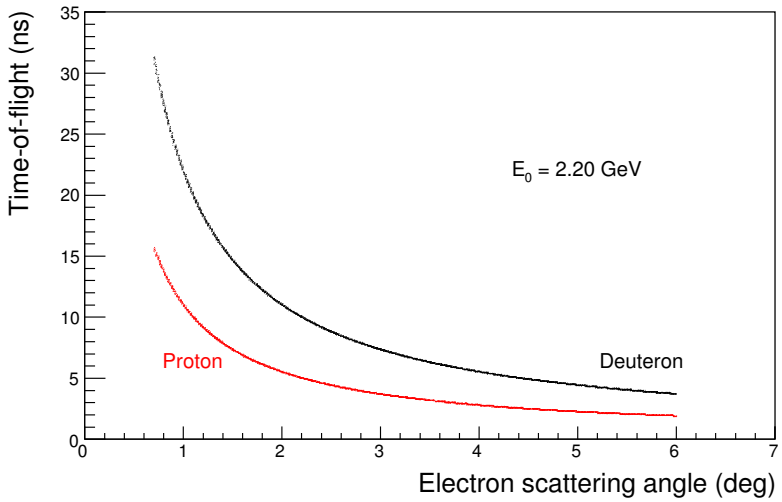

Figure 43: Time-of-flight *vs.* scattering angle for elastic $ed \to ed$ and $ep \to ep$ processes at an incident beam energy of 2.2 GeV. (ed and ep scattering are shown together for comparison only)

criteria in this event selection process will be time-of-flight difference between the veto counters on front of the Hycal calorimeter and the recoil detector. The time-of-flight resolution shown in Figure 41 assumes 1 ns time resolution for the Si-detectors and for the scintillator veto counters. Knowing the position of the scattered electrons from the GEM detectors, one can easily improve the resolution to $\simeq 0.5$ ns for the veto counters.

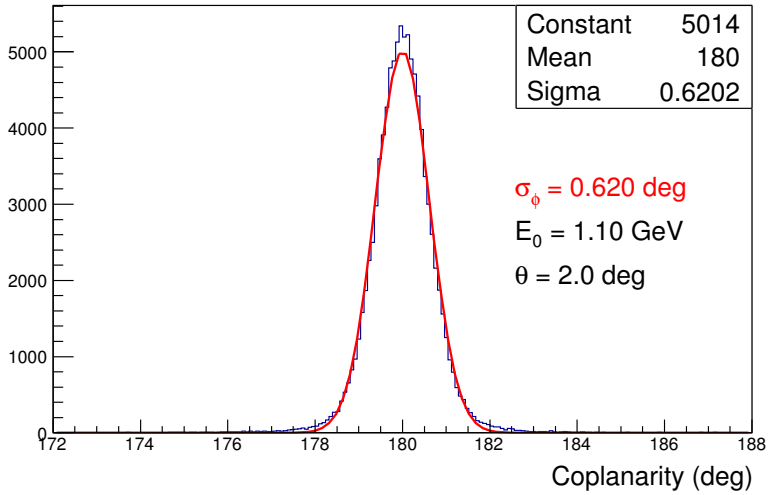

Figure 44: The simulated coplanarity distribution in the azimuthal direction, $\varphi_{e_1} - \varphi_{e_2}$, of the two electrons in Møller scattering at $E_0 = 1.1$ GeV. The minimum scattering angle cut implemented is $\theta_e \geq 0.7^\circ$.

Figures 42 and 43 show the time-of-flight differences between elastically scattered deuteron from $e - d$ process and elastic protons from $e - p$ for both energies of the incident beam. As it is seen, even with this conservative time resolution these two elastic processes can be safely separated within the projected scattered angular range.

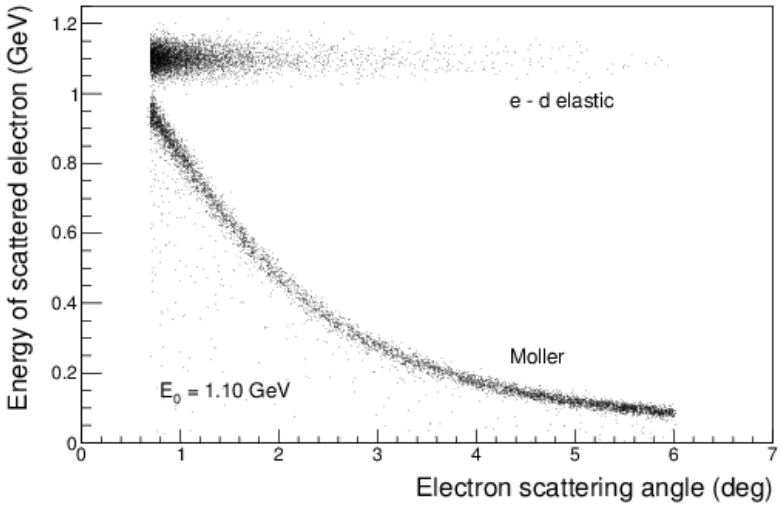

Figure 45: The simulated energy *vs.* scattering angle distribution of ed elastic and Møller scattered electrons at $E_0 = 1.1$ GeV. Internal and external radiative events have been included for the Møller scattering. For the 1.1 GeV case the electrons from the two processes can be clearly identified starting from $\theta_e = 0.7^\circ$.

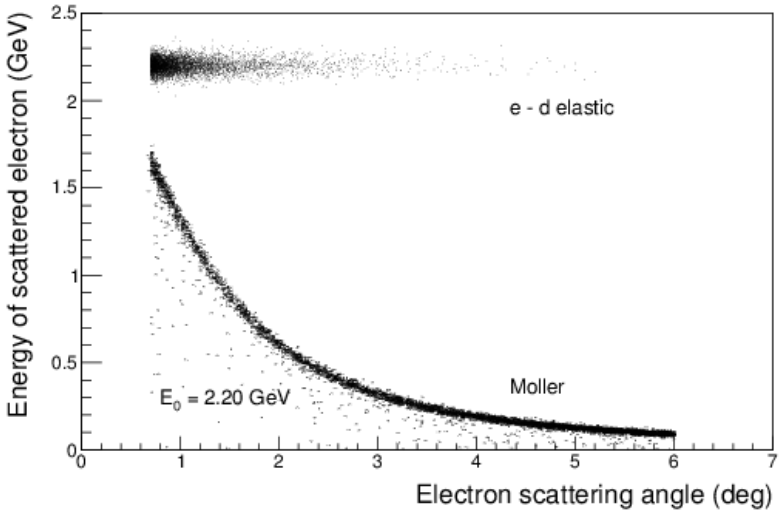

Figure 46: The simulated energy *vs.* scattering angle distribution of ed elastic and Møller scattered electrons at $E_0 = 2.2$ GeV. Internal and external radiative events have been included for the Møller scattering. For the 2.2 GeV case, no minimum scattering angle cut on θ_e (inside the HyCal acceptance) is required here to clearly identify the electrons from the two processes.

6.2.2 Resolutions for the Møller scattering

Similar to $ed \rightarrow ed$ scattering, the *"elasticity"* $(E_0 - (E_1 + E_2))$ is the number one criterion for the Møller scattering event selection. Since the energy of both of the scattered electrons will be measured by the HyCal calorimeter, the resolution in this quantity is practically the same as that for the ed scattering (Figures 37 and 38).

The co-planarity of two scattered electrons (ignoring the radiative effects) ($\varphi_{e_1} - \varphi_{e_2} = \pi$) is another

important criterion for the Møller event selection process. Figure 44 shows an excellent resolution in the co-planarity of the two scattered electrons measured by the two GEM detectors.

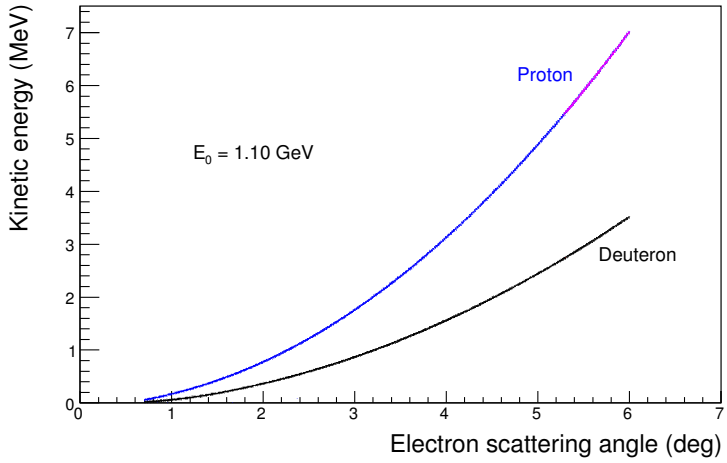

Figure 47: The simulated kinetic energy *vs.* electron scattering angle distribution of deuterons from ed elastic scattering and protons from ep elastic scattering at $E_0 = 1.1$ GeV. The protons that pass through the thin Si sensor are shown in magenta for protons. None of the deuterons can pass through the thin sensor. (ed and ep scattering are shown together for comparison only)

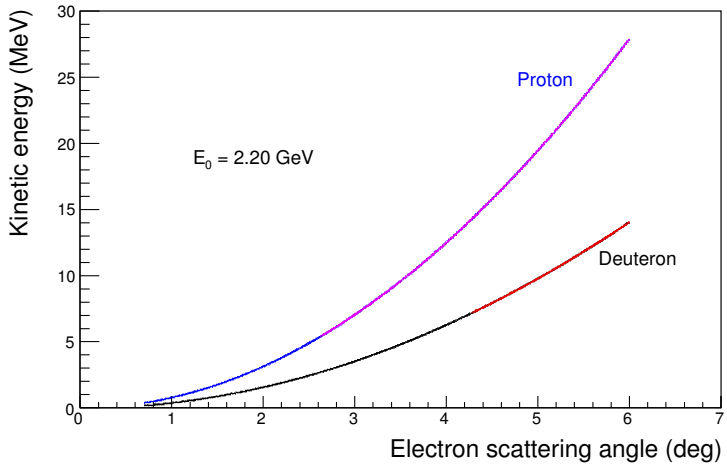

Figure 48: The simulated kinetic energy *vs.* electron scattering angle distribution of deuterons from ed elastic scattering and protons from ep elastic scattering at $E_0 = 2.2$ GeV. The protons that pass through the thin Si sensor are shown in magenta for protons and red for deuterons. (ed and ep scattering are shown together for comparison only)

A clear identification of the ed elastic scattering electrons from the Møller electrons requires that the tails of their energy distribution do not have any significant overlap. This condition can be achieved by requiring that the polar scattering angles of the electrons are above a certain minimum value. Figure 45 shows that above $\theta_e = 0.7^\circ$ the electrons from the two processes can be cleanly separated for $E_0 = 1.1$ GeV. A similar plot for $E_0 = 2.2$ GeV is shown in Fig. 46. Here, the ed elastic scattered electrons are separated from the Møller scattered electrons for all polar angles accepted by the HyCal calorimeter ($\theta_e > 0.5^\circ$. At

this stage of the simulations the radiative effects in ed scattering have not been included in the GEANT4 code, but, they are included for the Møller processes. We have used an event generator, developed for the PRad experiment, that includes radiative effects for the Møllerscattering and the $ep \to ep$ processes [36]. We are in the process of adapting the same formalism into the new event generator for the $ed \to ed$ process. The updated simulation results will be reported separately.

6.3 Proton and deuteron identification

The kinetic energy of the recoiling deuteron from the elastic ed scattering and the recoiling protons from ep elastic scattering are shown in Fig. 47 for electron beam energy of 1.1 GeV and Fig. 48 for 2.2 GeV. The protons from the electro-disintegration of deuteron have a similar range in energy. The highest energy protons and deuterons that can pass through the thin Si sensor into the thick Si sensor are also shown in magenta for the protons and red for the deuterons. At 1.1 GeV none of the deuterons can pass through the thin Si sensor. A Geant4 based Monte Carlo simulation of the experiment (detailed in Sec. 7.2) was used to simulate the energy deposited in the two layers of the recoil detector (described in Sec. 5.3).

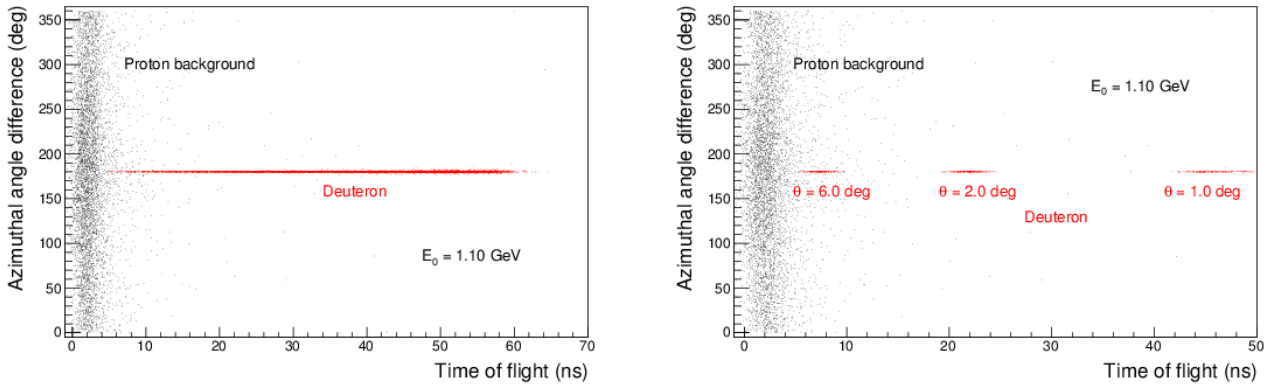

Figure 49: The distribution of $\Delta\phi$ angle from the GEM and the recoil detectors *vs.* time-of-flight difference between the recoil detector and the veto counters, for the deuterons from ed elastic scattering (red) and protons from deuteron disintegration (black) for $E_0 = 1.1$ GeV. All events with electron scattering angles between 0.7° and 6°(left) and events with electron scattering angles of 1°, 2° and 6° (right) are shown.

The deuteron electro-disintegration was also simulated along with the ed elastic and ep elastic scattering processes. The rate of electro-disintegrated protons was approximated as;

$$N(ed \to np) \simeq N_{\gamma*} \times \Delta\sigma(\gamma d \to np) \times N_{target},$$

where $N_{\gamma*}$ is the number of virtual photons, which for this thin target ($\sim 10^{-7}$ r.l.) can be calculated as $N_{\gamma*} \simeq 0.02 \times N_e$, where N_e is the number of electrons. The photo-disintegration cross section , $\Delta\sigma(\gamma d \to np)$ was taken to be 4 mb. With that;

$$N(ed \to np) \simeq 0.02 \times 6.25 \times 10^{10} \times 4 \times 10^{-27} \times 2 \times 10^{18} = 10 \text{ events/s}$$

As shown in Sec. 9, the rate for elastic $ed \to ed$ events is expected to be $\simeq 173$ events/s.

In the Monte Carlo simulation the outgoing angle of the proton and the spectator neutron is generated uniformly over the full angular phase space. The relative energy of the np system after disintegration is defined as $E_{np} = W - m_p - m_n$, where W is the invariant mass of the final state. The E_{np} is generated uniformly from 0 up to 100 MeV. The distribution of azimuthal angle difference $\Delta\phi$ as measured by the

GEM and the recoil detectors *vs.* time-of-flight difference between the recoil detector and the veto counters, for the deuterons from ed elastic scattering (red) and protons from deuteron disintegration (black) for $E_0 =$ 1.1 GeV, are shown in Fig. 49. The left panel is for all angles, while the right panel is for 1°, 2° and 6° angles only. A time-of-flight resolution of 1 ns is sufficient to distinguish the deuterons from the protons produced by the deuteron break-up reaction, for all angles except for the highest angles.

We will also select events by the $\left(\frac{dE}{dx}\right)$ detected in the first layer (thin Si sensor) and the ΔE detected by the second layer (thick Si sensor, see Fig. 50). Combination of these two criteria will clearly separate the ed elastic events from the deuteron breakup process.

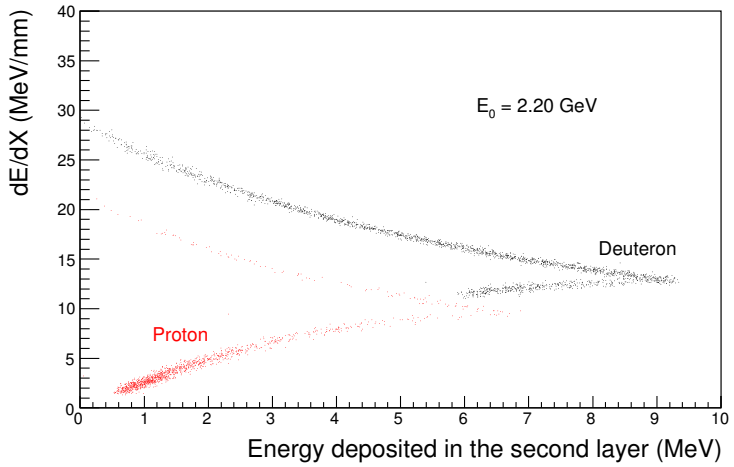

Figure 50: The energy loss in the thin Si detector *vs.* the energy deposited in the second (thick) Si detector for deuterons from ed elastic scattering and protons from electro-disintegration of the deuteron at $E_0 = 2.2$ GeV. These are only for events that can pass through the first (thin) silicon sensor.

7 Extraction of Deuteron Charge Radius

7.1 The method

As it is described in Sec. 2.1 the deuteron rms charge radius can be extracted from the slope of the charge form factor at the Q^2 = 0 limit (Eq. 3). Therefore, quite naturally, in order to extract the deuteron charge radius one needs to measure the $ed \rightarrow ed$ elastic differential cross section at lowest Q^2 values possible (Eq. 1). On the other hand, in order to have a reliable extraction of the slope a data set with a relatively larger Q^2 range is also required.

At very low Q^2 range the contributions to the cross sections from the magnetic (G_{Md}) and quadrupole (G_{Qd}) form factors are kinematically suppressed (Eq. 3). Therefore, for the small Q^2 range ($\sim 10^{-4} - 10^{-2}$ $(\mathrm{GeV/c})^2$) one can safely ignore the contributions from the other form factors and extract the charge form factor (G_{Cd}) *vs.* Q^2 from the measured elastic differential cross sections (Eq. 1,3). In this proposed experiment we will also cover relatively larger Q^2 range ($\sim 10^{-2} - 10^{-1}$ $(\mathrm{GeV/c})^2$). For the high Q^2 portion of the data, we will use the recent world-averaged values for the magnetic and quadrupole form factors, in order to include them in the fitting procedure to extract the charge radius.

In conclusion, in this proposed experiment the deuteron charge form factor, G_{Cd}, will be extracted from the measured $ed \rightarrow ed$ elastic cross sections *vs.* Q^2. Then the slope of G_{Cd} *vs.* Q^2 at this very low Q^2 range will determine the rms deuteron charge radius, r_d.

Typically, all $ed \rightarrow ed$ scattering experiments have been performed with magnetic spectrometers, by implementing liquid (or gas) deuterium targets. Such methods arguably have a limited accuracy in absolute values of the measured cross sections ($\sim 2\%$), unless measured relative to the $ep \rightarrow ep$ process performed with the same setup (with two different targets) [23]). However, the $ep \rightarrow ep$ cross sections, measured so far by the same magnetic spectrometer method, are themselves known no better than $\sim 2\%$.

In this new experiment, similar to the PRad experiment performed by our collaboration last year, a new magnetic-spectrometer-free measurement is proposed using the PrimEx HyCal high resolution and large acceptance electromagnetic calorimeter. We will also use a deuterium gas flow target (similar to the PRad target), which in turn will allow an effective detection of extremely low energy ($\sim$ 1 MeV) recoiling deuterons with the proposed new cylindrical Si-strip detectors, located inside of the gas target (Sec. 5.3). As it was demonstrated by the PRad experiment, this method reaches to the extreme low Q^2 range ($\sim 10^{-4}$ $(\mathrm{GeV/c})^2$), and, at the same time, allows measurement of the $e^-e^- \rightarrow e^-e^-$ Møller scattering cross sections parallel to the main scattering process. Using the proposed setup, the $ed \rightarrow ed$ elastic cross sections will be measured by normalizing them to the Møller cross section. The Møller cross sections will be obtained from theoretical QED calculations within the particular experimental acceptance, taking into account the radiative effects (see Eq. 14). The requirement to detect the recoiling deuteron in this experiment will introduce an asymmetry in the target acceptance of these two elastic processes. However, measurement of the same ratio for the $ep \rightarrow ep$ and Møller processes performed with the hydrogen gas flow target, will cancel out this unknown effective target length (see Sec. 3.2).

7.2 Monte Carlo simulations

In order to investigate the uncertainties in the extraction of r_d, a full Monte Carlo simulation code based on GEANT4 package has been developed, which takes into account the realistic geometry of the experimental setup, including all detector resolutions. This program generates events based on theoretical cross sections which are then traced through the target and detection systems. The Monte Carlo generated events are then analyzed to reconstruct the "measured" differential cross sections. In this scheme one can obtain the uncertainties in r_d *vs.* detector resolutions, geometrical acceptances, misalignment of beam and experimental setup. Currently, this program accounts for the radiative processes inside of the gas target (external radiative corrections). However, the so called internal radiative corrections for the $ed \rightarrow ed$ scattering process are not yet included in this code. We are in the process of implementing a new event generator including all the radiative effects for the $ed \rightarrow ed$ scattering process, such that the sensitivity to these corrections in the extraction of the deuteron charge radius can be studied. The formalism is based on the radiative corrections for $ep \rightarrow ep$ process that was developed for the PRad experiment [36]. One important advantage of the calorimetric method over the traditional magnetic spectrometer method is that in this case we have a parallel measurement of the part of the radiative effects, related to target bremsstrahlung, and the so called hard radiative effects. This fact, will significantly reduce the effects of radiative corrections in this proposed experiment. The results from the fully implemented corrections in the Monte Carlo code will be reported prior to the proposal defense.

One of the tasks for these simulations was to estimate the uncertainty in the fitting procedure taking in account the geometrical acceptances and the resolutions of the setup. Figure 51 shows the extraction of the r_d from the Monte Carlo simulated data for the incident energy of $E_0 = 1.1$ GeV. The similar distribution including both energies is shown in Fig. 52.

Figure 53 is demonstrating the stability of the fitting procedure *vs.* input radius. Based on these simulations we conclude that, with the realistic detector resolutions the uncertainty in fitting is at the level of 0.2%.

To estimate the uncertainties of the radius extraction from the detector misalignment we artificially shifted the GEMs position by an amount of +1 and +2 mm in the event reconstruction stage. The results of

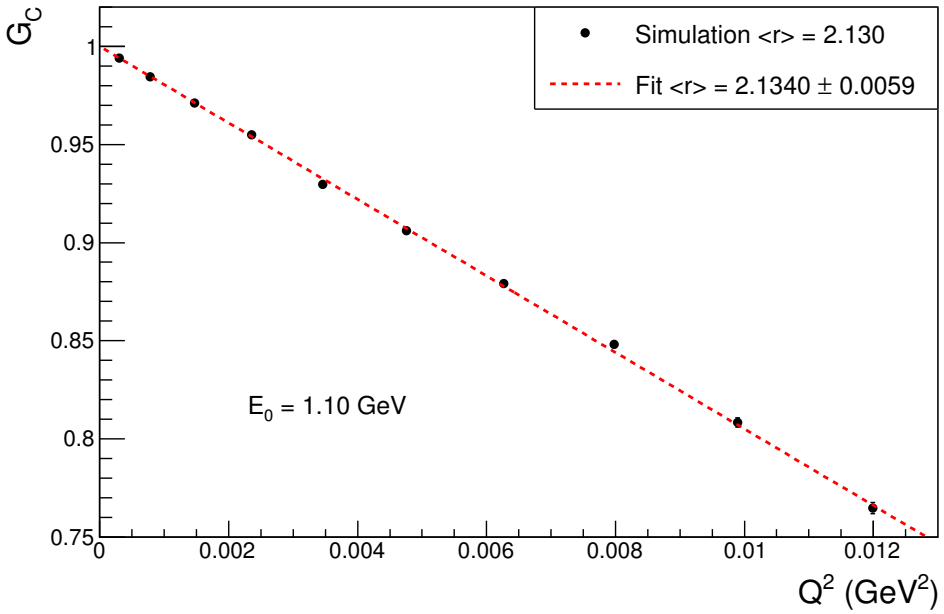

Figure 51: Extraction of G_{Cd} from the Monte Carlo generated data set for $E_0 = 1.1$ GeV for the input value of $r_d = 2.130$ fm. The error bars shown are statistical only ($\sim 0.2\%$).

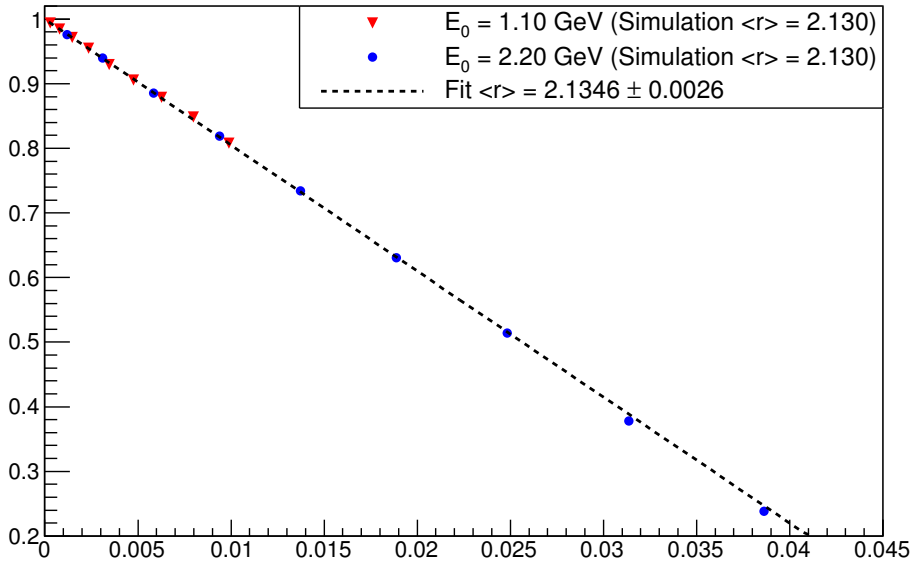

Figure 52: Extraction of G_{Cd} from the Monte Carlo generated data set for both energies, $E_0 = 1.1$ and 2.2 GeV, for the input value of $r_d = 2.130$ fm. The error bars shown are statistical only ($\sim 0.2\%$).

these simulations are shown in Figs. 54 and 55. In addition to engineering survey (uncertainty ~ 0.7 mm), the position alignment of the GEM detectors and the HyCal calorimeter will also be performed using the

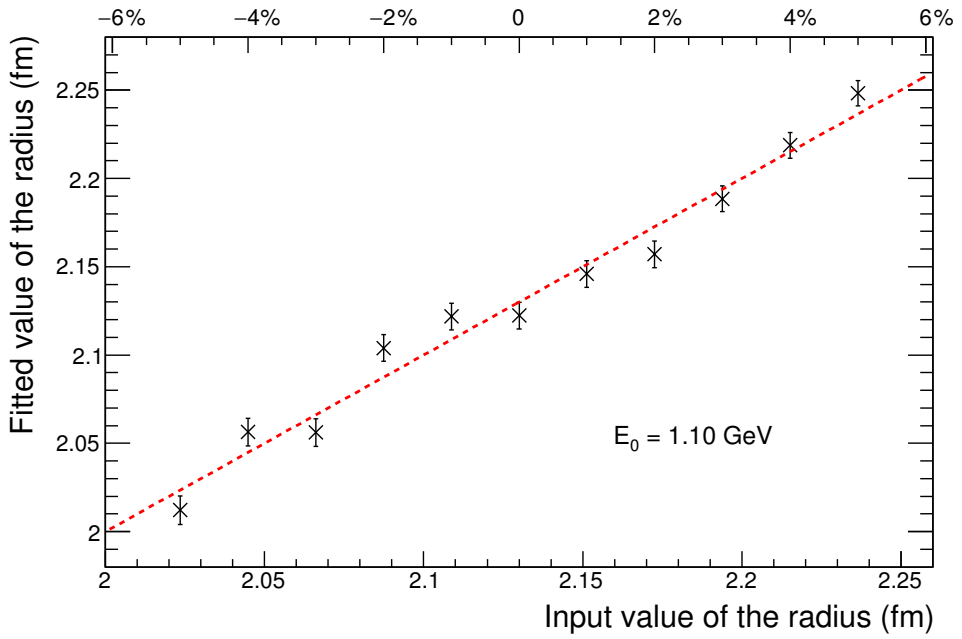

Figure 53: Stability of fitting procedure: extracted *vs.* input values of the deuteron charge radius for $E_0 = 1.1$ GeV beam energy. The statistical errors for these simulations are relatively larger than those in Figs. 52 and 51.

coplanarity of the Møller events. This experiment will have a large statistics for this type of events, and based on experience from the PRad experiment, it will allow alignment of the GEM detectors with an uncertainty of ∼0.2 mm and the HyCal with an uncertainty of ∼0.5 mm. With that, our simulations demonstrate that the contribution to the uncertainty of deuteron radius extraction from detector misalignments are less than 0.1%, and are thus not included in the error budget.

8 Statistics, event rate and beam time

The full Monte Carlo event sampling program was used to estimate the statistics and event rates for this proposal. As mentioned earlier this program samples both $ed \to ed$ and $e^-e^- \to e^-e^-$ processes according to their differential cross sections and traces the events through the target, vacuum scattering chamber, two GEM detectors and the HyCal calorimeter. The positions and energies of the secondary particles were sampled in GEM and HyCal according to their experimental resolutions described in Secs. 5.4, 5.6.

The deuterium gas target in this experiment will be very similar to the hydrogen gas flow target successfully commissioned and used in the PRad experiment last year. The projected thickness of the target is: $N_{\rm tgt} = 2 \cdot 10^{18}$ deuterium atoms/cm^2. We ran most of the PRad experiment with an incident electron beam intensity of $I_{\rm beam} = 10$ nA ($N_e = 6.25 \cdot 10^{10}\ e^-/{\rm s}$). The rates for the $ed \to ed$ elastic events in the experimental setup can be estimated by:

$$N_{ed} = N_e \cdot N_{\rm tgt} \cdot \Delta\sigma \cdot \varepsilon_{\rm geom} \cdot \varepsilon_{\rm det}\ ,$$

where $\Delta\sigma$ is the integrated elastic cross section at forward angles ($\theta_e = 0.7^\circ - 6.0^\circ$), accepted by the setup (1.38×10^{-27} cm^2); $\varepsilon_{\rm geom}$ is the geometrical acceptance of the setup. For these calculations, as a simplification, we assumed that the detection efficiency is $\varepsilon_{\rm det} \approx 1$ and $\varepsilon_{\rm geom} \approx 1$. With all that, the

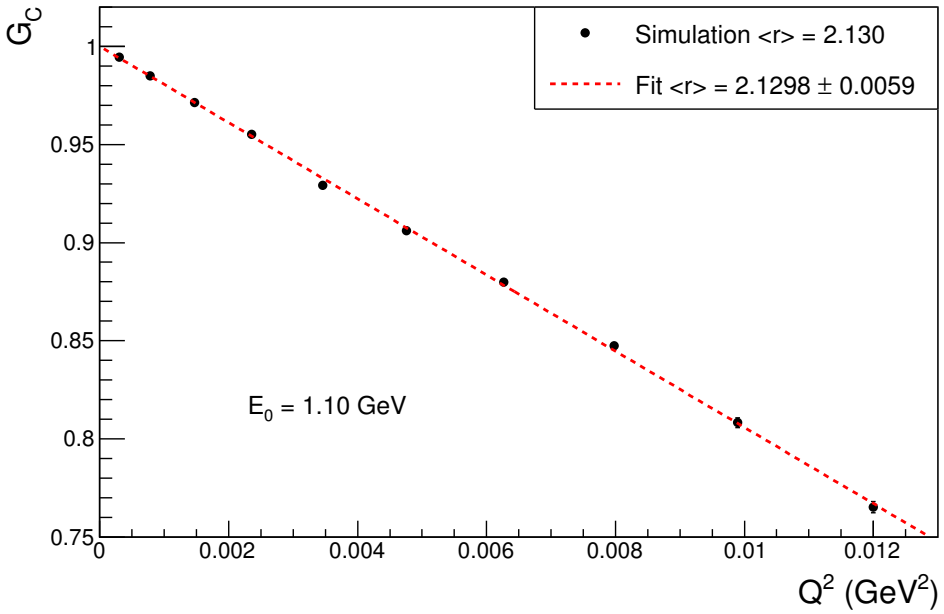

Figure 54: Extracted radius when the GEM X-coordinate is artificially shifted by +1 mm in the event reconstruction stage.

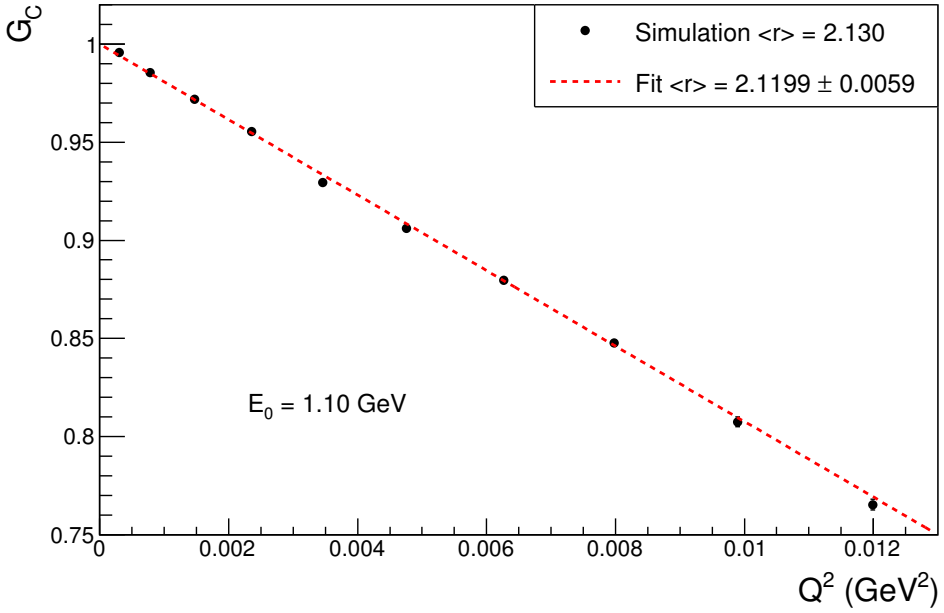

Figure 55: Extracted radius when the GEM X-coordinate is artificially shifted by +2 mm in the event reconstruction stage.

integrated rate of events from the $ed \to ed$ process is:

$$\begin{aligned} N_{ed} &= 6.25 \cdot 10^{10} \cdot 2 \cdot 10^{18} \cdot 1.38 \cdot 10^{-27}\ events/\mathrm{s} \\ &\simeq 173\ events/\mathrm{s} \\ &\simeq 14.9\mathrm{M}\ events/\mathrm{day}\ . \end{aligned}$$

This is a high integrated statistics per day for the forward angles. However, due to $\sim 1/\sin^4(\theta/2)$ nature of the scattering process, as well as the deuteron form factors, most of these events will be populated in the extreme forward angles ($\theta_e \sim 0.7^\circ$) of our acceptance range. Therefore, in order to achieve a sub-percent level ($\simeq 0.8\%$) statistical uncertainty even for the last Q^2 bin ($\theta_e = 5.95^\circ - 6.00^\circ$), we have to run for 8 days at this $E_0 = 1.1$ GeV energy setting: Therefore, with $I_{\rm beam} = 10$ nA and $N_{\rm tgt} = 2 \cdot 10^{18}$ deuterium atoms/cm^2, eight days of run time will be sufficient to get the required high statistics (sub-percent) for all Q^2 points including the very last bin, $Q^2 = 1.311 \pm 0.011 \cdot 10^{-2}$ (GeV/c)^2.

$$\begin{aligned} N_{ed}(\theta_e = 5.95^\circ - 6.00^\circ) &= 6.25 \cdot 10^{10} \cdot 2 \cdot 10^{18} \cdot 1.83 \cdot 10^{-31}\ events/\mathrm{s} \\ &\simeq 0.023\ events/\mathrm{s} \\ &\simeq 15,830\ events/8\ \mathrm{days}\ . \end{aligned}$$

The $e^-e^- \to e^-e^-$ Møller cross section is significantly higher than the $ed \to ed$ cross section for the same incident beam energies. Under same experimental conditions (beam intensity and target thickness) the event rate for this process will be:

$$\begin{aligned} N_{e^-e^-}(\mathrm{coin.}) &= 6.25 \cdot 10^{10} \cdot 2 \cdot 10^{18} \cdot 0.68 \cdot 10^{-24} \cdot 0.0048\ e^-e^-/\mathrm{s} \\ &\simeq 400\ e^-e^-/\mathrm{s} \\ &\simeq 34.6\mathrm{M}\ e^-e^-/\mathrm{day}\ . \end{aligned}$$

As it was stated earlier, we also request to have a separate run with $E_0 = 2.2$ GeV beam energy to increase the Q^2 range for a more stable fit of the G_{Cd} *vs.* Q^2 to extract the deuteron charge radius. The Møller cross section is inversely proportional to the beam energy, so we will have twice less cross section with the $E_0 = 2.2$ GeV beam. On the other hand, the geometrical acceptance of the $e^-e^- \to e^-e^-$ reaction also increases with the energy. With all that, the Møller rate at $E_0 = 2.2$ GeV will be of the same order as for the first energy. For the $ed \to ed$ elastic scattering process the cross section drops as $1/E^2$ and, therefore, all rates for the 2.2 GeV run will be about four times less than for those at 1.1 GeV. Considering all these factors and optimizing the requested beam time, we request 16 days of run time for the $E_0 = 2.2$ GeV beam. This will provide sub-percent statistics for most part of the Q^2 range, except for the few points at larger Q^2 where we will have statistical uncertainties still close to 1%.

At the forward electron scattering angles of this experiment, the estimated π^+/e ratio is less than $\sim 10^{-3}$ [42]. For these low hadronic rates the HyCal electromagnetic calorimeter, which has a π/e rejection capability of $\sim 10^{-2}$, makes the hadronic background negligible. Thess estimated were confirmed during the PRad experiment.

In summary, we are requesting 8 days of run time for the $E_0 = 1.1$ GeV beam and 16 days for the $E_0 = 2.2$ GeV beam to provide sufficient statistics for the precision extraction of the deuteron charge radius. We will need 3.5 more days for experimental setup checkout, tests and calibration of the GEM/HyCal detectors, 2 days for commissioning and integration of the new Si-strip cylindrical recoil detector. For the calibration of this new recoil detector we need 3 days with hydrogen gas in the target. The energy change from one-pass to two-pass typically requires about half-a-day. To control the experimental background originated from electron beam halo hitting the outside engineering structure of the gas flow target and exclude the background events from the residual beam line gas, we will also need total of 6 days of empty target runs. These runs will be periodically performed during the entire time of the experiment. With that, we are requesting a total of 39 days to perform this experiment and extract the deuteron charge radius with a sub-percent precision.

Table 3: Beam time request.

	Time (days)
Setup checkout, tests and calibration	3.5
Recoil detector commissioning	2
Recoil detector calibration with hydrogen gas	3
Statistics at 1.1 GeV	8
Energy change	0.5
Statistics at 2.2 GeV	16
Empty target runs	6
Total	39

9 Estimated uncertainties

These two processes, $ed \to ed$ and $e^-e^- \to e^-e^-$ Møller, that we are aiming to measure simultaneously in this proposed experiment, are the most probable two electromagnetic processes at these very forward angles. Based on the rates estimated in Sec. 8, we expect to have enough statistics within the requested beam time, to provide statistical uncertainties on the level of 0.2% for each Q^2 bin, on average. For the lower Q^2 bins, this number would be significantly less than 0.2%. That will provide 0.2% level uncertainty in the fitting process (Sec. 8). With that, the major concern for this type of experiment, is the control of the systematic uncertainties, and their contribution to the final uncertainty of the extracted deuteron charge radius. We are convinced that the proposed experiment with its: (1) possibility to reach very low Q^2 range; (2) with normalizing the ed cross sections to a well known QED process, like the Møller scattering; (3) very low density windowless deuterium gas target to minimize the physics background processes; and (4) detection of the recoil deuterons to insure the elasticity in the extracted cross sections, is currently the most optimized ed measurement to extract the deuteron charge radius with a sub-percent precision.

The following list is itemizing the expected sources of systematic uncertainties in this proposed experiment: (1) uncertainty in the event selection process, including the radiative corrections; (2) calibration of the recoil detector and measurement of the geometrical acceptance with the ep elastic scattering process; (3) misalignment in position reconstruction (GEM/HyCal detectors); (4) misalignment of beam position and angle on the target; (5) misalignment in calorimeter energy calibration.

Based on our experience in analyzing the PRad experimental data, we estimate 0.3% level uncertainty in the event selection process. As it is described in Sec. 7.1 the calibration of the recoil detector and measurement of its geometrical acceptance will be performed by a separate measurement of $ep \to ep$ elastic scattering process using the hydrogen gas in the target with similar conditions (like the PRad experiment). The uncertainty on this quantities are being estimated to be not more than 0.3%. The position of the GEM detectors and the HyCal calorimeter on the beam line will be determined by engineering survey with an accuracy of ~ 0.7 mm. In addition, the coplanarity of the $e^-e^- \to e^-e^-$ process will be used in offline analysis to obtain a finer definition of the position and angle on the calorimeter ($\simeq$0.5 mm) . The position of the beam on the target will be controlled on the level of less than 0.2 mm during the entire period of the experiment. The energy calibration of the calorimeter will be performed by the Hall B photon tagger at $E_0 =$ 1.1 or 2.2 GeV. The energy uncertainty of the tagger is at the level of $\sim 10^{-3}$. Therefore, its contribution to

the event selection uncertainty is negligible. The Q^2 values in this experiment will be defined by the beam energy and scattered angle very accurately defined by the two GEM detectors.

As it is described in Sec. 3, the ed cross sections will be measured with respect to the Møller. Therefore, the two major systematic uncertainties, most typical for other ed experiments, will cancel out in the ratio. The remaining systematic uncertainties will depend on the method with which we identify the Møller events and, therefore, the cross sections for that particular Q^2 bin. The single-arm method, described in Sec. 3.4.1, is the best way to further cut down the sources of the systematic uncertainties in the simulation of the Møller cross section for a particular Q^2 bin since it will be calculated in the same ed acceptance. With this method the uncertainty contribution to the event selection is estimated to be on a 0.3% level.

For the two other Møller event selection methods, two more items are remaining in the determination of the ed cross sections; the partially different geometrical acceptances, and, the detection efficiencies. In this experiment we will measure the detection efficiencies of all detectors during the experimental setup calibration runs. The differences of the detection efficiencies for the different part of the detection system, based on our previous experiences, is expected to be rather small and therefore, it will not contribute significantly in the final uncertainty.

Table 4 is summarizing the estimated uncertainties in this proposed experiment together with the total expected uncertainty of 0.5% (added in quadrature).

Table 4: Total estimated uncertainty.

Item	Uncertainty (%)
Statistical uncertainty	0.1
Event selection (including rad. corr.)	0.3
Acceptance in recoil detector	0.3
Fitting procedure	0.2
Ratio in acceptance and det. eff.	0.2
Total	0.5

10 Related Experiments

In 2014 a new deuteron form factor measurement was carried out at MAMI by the A1 collaboration [43]. This is a magnetic spectrometer based experiment using a liquid deuterium target and covered a Q^2 range of 2.3×10^{-3} - 0.3 $(\mathrm{GeV/c})^2$. The data were collected for 200 different kinematic points over this Q^2 range. The data are still being analyzed and the radius extraction will take place in the near future. A typical missing energy spectrum for this experiment is shown in Fig. 56. The events beyond $\Delta E' = 2.2$ MeV are from deuteron breakup while the events at $\Delta E' < 0$ are from the target cell wall.

The proposed experiment has several advantages compared to MAMI experiment; (1) it will access a value of Q^2 that is one order of magnitude smaller; (2) it will use a windowless gas flow target which avoids large contributions from the cell wall; (3) the detection of the recoil deuteron will help eliminate background from the deuteron breakup; (4) the cross section will be calibrated against a well known QED process. Note that access to the lowest Q^2 achievable is even more critical for the deuteron radius extraction than for the proton.

There are also plans at MAMI to build a new "Universal Detector" consisting of a time projection chamber filled with hydrogen or other gaseous light nuclei and a forward tracking detector that can detect

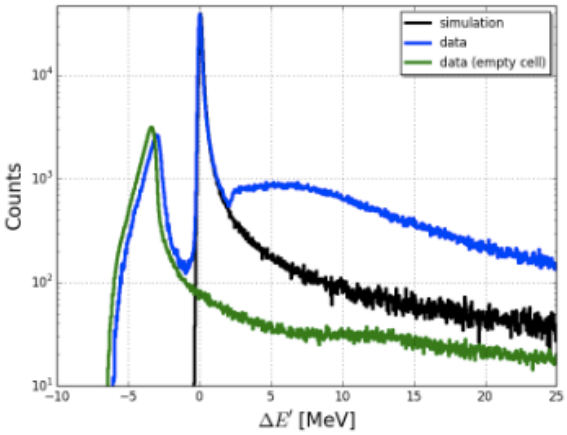

Figure 56: Distribution of elastic ed scattering data (blue) as a function of the $\Delta E' = E'(\theta_e) - E'$, along with simulation (black) and empty target events (green) for $E_e = 315$ MeV and θ_e =23.6°. The events beyond $\Delta E' = 2.2$ MeV are from deuteron breakup while the events at $\Delta E' < 0$ are from the target cell wall. The figure is reproduced from Ref. [43].

recoil fragments in the final state. A research program to measure the cross-section of elastic electron-light-nuclei scattering at low Q^2 with the simultaneous detection of the recoil fragment and the scattered electron with this new Universal Detector was submitted in a letter of intent to the MAMI PAC in 2016 [44]. However, the initial effort will be focused on measuring the electron-proton scattering cross section.

In summary, currently to the best of our knowledge, there are no other experiments planning to measure the deuteron radius at this time.

11 Summary

After about seven years of intense theoretical and experimental efforts the well-known *"proton charge radius puzzle"* remains unresolved. In addition to this, over the last year the same CREMA collaboration at PSI has succeeded in performing new high precision measurements of the deuteron rms charge radius using spectroscopy of muonic deuterium atoms, which demonstrated about 7 σ discrepancy with the long-established CODATA world-average value. This fact created a new *"deuteron charge radius puzzle"* in nuclear and hadronic physics.

We propose to perform a new high precision $ed \to ed$ elastic cross section measurement at very low scattering angles, $\theta_e = 0.7^\circ - 6.0^\circ$, using the same PRad method and experimental setup, to extract the deuteron charge radius with high precision. The proposed experiment will have two major modifications *vs.* PRad:

(1) To ensure the elasticity in the ed-scattering process we will add a low energy Si-based cylindrical recoil detector inside the windowless gas flow target cell;

(2) The tracking capability for the vertex reconstruction will be significantly improved by adding the second GEM detector in front of the HyCal calorimeter. That will critically improve the control of beam line background, especially at very small scattering angles ($\theta_e \simeq 1^\circ$).

Similar to PRad, in this new experiment the systematic uncertainties in the extracted deuteron charge radius ($\simeq 0.4\%$) will be controlled by: (1) normalizing the ed cross sections to a well known QED process - Møller scattering; (2) reaching very forward scattering angles for the first time in ed experiments while covering a large enough Q^2 range ($2{\cdot}10^{-4} - 5{\cdot}10^{-2}$ $(\mathrm{GeV/c})^2$) for the extraction of the slope in deuteron charge form factor - G_{Cd}; (3) measuring the cross section over the large Q^2 range in a single setting of the experimental setup; (4) reducing the experimental background typical for all previous $ed \to ed$ experiments by using a windowless, low density deuterium gas flow target, together with a new cylindrical Si-strip recoil detector.

With that, we request 39 days of beam time in Hall B to extract the deuteron charge radius with a 0.5% total uncertainty to address the recently developed *"deuteron charge radius puzzle"* in nuclear and hadronic physics.

References

[1] P. J. Mohr, B. N. Taylor, D. B. Newell, Rev. Mod. Phys. **84**, 1527 (2012).

[2] R. Pohl, *et al.*, Nature **466**, 213 (2010).

[3] A. Antognini, *et al*, Science **339**, 417 (2011).

[4] R. Pohl, *et al.*, Science **353**, 669 (2016).

[5] R. Phol, R. Gilman, G. A. Miller, K. Pachucki, Ann. Rev. Nuc. Part. Sci. **63**, 175 (2013).

[6] C. E. Carlson, Prog. Part. Nucl. Phys. **82**, 59 (2015).

[7] A. Huber, *et al.*, Phys. Rev. Lett. **80**, 468 (1998).

[8] C. G. Parthey, *et al.*, Phys. Rev. Lett. **104**, 233001 (2010).

[9] U. D. Jentschura, *et al.*, Phys. Rev. A **83**, 042505 (2011).

[10] R. Pohl, *et al.* Metrologia **54**, L1 (2017).[arXiv:1607.03165].

[11] C. W. Wang Int. Jour. Mod. Phys. E **3**, 821 (1994).

[12] D. Dricky and L. Hand, Phys. Rev. Lett. **9**, 521 (1962).

[13] M. .N. Rosenbluth, Phys. Rev. **79**, 615 (1950).

[14] V. Z. Jankus, Phys. Rev. **102**, 1586 (1956).

[15] M. Gourdin, Nuo. Cim. **28**, 533 (1963); **32**, 493 (1964).

[16] J. A. McIntyre and S. Dhar, Phys. Rev. **106**, 1074 (1957).

[17] G. H ohler *et al.*, Nucl. Phys. B **114**, 505 (1976).

[18] G. G. Simon, Ch. Schmitt and V. H. Walther, Nucl. Phys. A **364**, 285 (1981).

[19] L. Koester, W. Nistler and W. Waschkowski, Phys. Rev. Lett. **36**, 1021 (1976).

[20] I. Sick and D. Trautmann, Nucl. Phys. A **637**, 559 (1998).

[21] R. W. Berard *et al.*, Phys. Lett. B **47**, 355 (1973).

[22] S. Platchkov *et al.*, Nucl. Phys. A **510**, 740 (1990).

[23] G. G. Simon, Ch. Schmitt, F. Borkowski and V. H. Walther, Nucl. Phys. A **333**, 381 (1980).

[24] A. Bachmann, H. Henning and P. U. Sauer, Few Body Syst. **21**, 149 (1996).

[25] T. Herrmann and R. Rosenfelder, Eur. Phys. J. A**2**, 29 (1998).

[26] B. Desplanques, Phys. Lett. B **203**, 200 (1988).

[27] I. Sick and D. Trautmann, Phys. Lett. B **375**, 16 (1996).

[28] J. L. Friar, J. Martorell and D. W. L. Sprung, Phys. Rev. A **56**, 5173 (1997).

[29] K. Pachucki *et al.*, J. Phys. B **29**, 177 (1996).

[30] G. W. Erickson and D. R. Yennie, Ann. Phys. **35**, 271 (1965).

[31] T. Udem, Ph.D. thesis, *Ludwig-Maximilians Universit at*, Munich, Germany (1997).

[32] M. Weitz, F. Schmidt-Kaler and T. W. H ansch, Phys. Rev. Lett. **68**, 1120 (1992).

[33] A. Huber, *et al.*, Phys. Rev. Lett. **80**, 468 (1998).

[34] C. G. Parthey, *et al.*, Phys. Rev. Lett. **104**, 233001 (2010).

[35] U. D. Jentschura *et al.*, Phys. Rev. A **83**, 042505 (2011).

[36] I. Akushevich, H. Gao, A. Ilyichev and M. Meziane, EPJA **51**, 1 (2015).

[37] PrimEx Conceptual Design Report, 2000 (`http://www.jlab.org/primex/`).

[38] I. Larin *et al.*, (PRIMEX Collaboration), Phys. Rev. Lett. **106**, 162303 (2011).

[39] CLAS12 Technical Design Report, 2008 (`https://www.jlab.org/Hall-B/clas12_tdr.pdf`).

[40] CLAS12 Detector documentation (`http://clasweb.jlab.org/clas12offline/docs/detectors/html/svt/introduction.html`).

[41] M. Kubantsev *et al.*, AIP Conf. Proc. **867**, 51 (2006).

[42] A. Gasparian, M. Khandaker, H. Gao, and D. Dutta, JLAB Experiment E12-11-106 (2011) (`http://www.jlab.org/exp_prog/proposals/11/PR12-11-106.pdf`)

[43] B. S. Schlimme *et al.* EPJ Web of Conference, **113**, 04017 (2016).

[44] A. A. Vorobyov. Letter of intent for high precision measurement of the ep elastic cross section at small Q^2. 2016.